

# Luminosities and mass-loss rates of carbon stars in the Magellanic Clouds

M. A. T. Groenewegen,<sup>1\*</sup> P. R. Wood,<sup>2</sup> G. C. Sloan,<sup>3</sup> J. A. D. L. Blommaert,<sup>1</sup>  
 M.-R. L. Cioni,<sup>4</sup> M. W. Feast,<sup>5</sup> S. Hony,<sup>1†</sup> M. Matsuura,<sup>6,7</sup> J. W. Menzies,<sup>10</sup>  
 E. A. Olivier,<sup>10</sup> E. Vanhollebeke,<sup>1</sup> J. Th. van Loon,<sup>8</sup> P. A. Whitelock,<sup>5,10,11</sup>  
 A. A. Zijlstra,<sup>9</sup> H. J. Habing<sup>12</sup> and E. Lagadec<sup>9</sup>

<sup>1</sup>*Institute of Astronomy, University of Leuven, Celestijnenlaan 200D, B-3001 Leuven, Belgium*

<sup>2</sup>*Research School of Astronomy and Astrophysics, Australian National University, Cotter Road, Weston Creek, ACT 2611, Australia*

<sup>3</sup>*Department of Astronomy, Cornell University, 108 Space Sciences Building, Ithaca, NY 14853-6801, USA*

<sup>4</sup>*SUPA, School of Physics, University of Edinburgh, IFA, Blackford Hill, Edinburgh EH9 3HJ*

<sup>5</sup>*Astronomy Department, University of Cape Town, 7701 Rondebosch, South Africa*

<sup>6</sup>*APS Division, Department of Pure and Applied Physics, Queen's University Belfast, University Road BT7 1NN*

<sup>7</sup>*National Astronomical Observatory of Japan, Osawa 2-21-1, Mitaka, Tokyo 181-8588, Japan*

<sup>8</sup>*Astrophysics Group, School of Physical and Geographical Sciences, Keele University, Staffordshire ST5 5BG*

<sup>9</sup>*School of Physics and Astronomy, University of Manchester, Sackville Street, PO Box 88, Manchester M60 1QD*

<sup>10</sup>*South African Astronomical Observatory, PO Box 9, 7935 Observatory, South Africa*

<sup>11</sup>*NASSP, Department of Mathematics and Applied Mathematics, University of Cape Town, 7701 Rondebosch, South Africa*

<sup>12</sup>*Sterrewacht Leiden, Niels Bohrweg 2, 2333 RA Leiden, The Netherlands*

Accepted 2006 December 19. Received 2006 December 18; in original form 2006 November 8

## ABSTRACT

Dust radiative transfer models are presented for 60 carbon stars in the Magellanic Clouds (MCs) for which 5–35  $\mu\text{m}$  *Spitzer* infrared spectrograph (IRS) spectra and quasi-simultaneous ground-based *JHKL* photometry are available. From the modelling, the luminosity and mass-loss rate are derived (under the assumption of a fixed expansion velocity and dust-to-gas ratio), and the ratio of silicon carbide (SiC) to amorphous carbon (AMC) dust is also derived. This ratio is smaller than observed in Galactic carbon stars, as has been noted before. Light curves for 36 objects can be retrieved from the massive compact halo object (MACHO) and optical gravitational lensing experiment (OGLE) data bases, and periods can be derived for all but two of these. Including data from the literature, periods are available for 53 stars.

There is significant scatter in a diagram where the mass-loss rates are plotted against luminosity, and this is partly due to the fact that the luminosities are derived from single-epoch data. The mass-loss rates for the MC objects roughly scatter around the mean relation for Galactic C-stars.

The situation is better defined when the mass-loss rate is plotted against pulsation period. For a given period, most of the Large Magellanic Cloud (LMC) and Small Magellanic Cloud (SMC) stars have mass-loss rates that are in agreement with that observed in Galactic carbon stars (under the assumption that these objects have an expansion velocity and dust-to-gas ratio typical of the mean observed in Galactic carbon Miras).

For some SMC sources only, the IRS spectrum at longer wavelengths falls clearly below the model flux predicted by a constant mass-loss rate. An alternative model with a substantial increase of the mass-loss rate to its present-day value over a time-scale of a few tens of years is able to explain the spectral energy distribution (SED) and IRS spectra of these sources. However, the probability to have two such cases in a sample of 60 is small, and makes this not a likely explanation (and testable by re-observing these objects near the end of the lifetime of *Spitzer*). Alternative explanations are (ad hoc) changes to the dust emissivity at longer wavelengths, and/or deviations from spherical symmetry.

\*E-mail: groen@ster.kuleuven.be

†Present address: Service d'Astrophysique, Bat.609 Orme des Merisiers, CEA Saclay, 91191 Gif-sur-Yvette, France.

**Key words:** circumstellar matter – stars: AGB and post-AGB – stars: mass-loss – Magellanic Clouds – infrared: stars.

## 1 INTRODUCTION

Almost all stars with initial masses in the range  $0.9\text{--}8 M_{\odot}$  will pass through the asymptotic giant branch (AGB) phase, which is the last stage of active nuclear burning before they become post-AGB stars, Planetary Nebulae and finally White Dwarfs. The main characteristics of the AGB are (i) the active dredge-up of the products of nucleosynthesis (mainly carbon, nitrogen, *s*-process elements) which allows an AGB star to make the transition  $M \rightarrow S \rightarrow C$  in spectral type depending on the number of so-called thermal pulses and subsequent dredge-up events, and (ii) significant mass loss, induced by stellar pulsation and radiation pressure acting on dust grains, which results in a huge expanding molecular and dust shell around the star. The combination of nucleosynthesis and heavy mass loss makes AGB stars the most important contributor to the enrichment of the interstellar medium (ISM) in dust and many atomic species.

The dust which forms around these cool AGB stars absorbs stellar light below  $\lesssim 1 \mu\text{m}$  and re-emits it in the infrared (IR). At the very end of the AGB, the heavy mass loss makes this effect so prominent that stars become faint or invisible in the optical and very prominent emitters in the near-IR and mid-IR.

The fact that the process of significant dust production also occurs at metallicities below solar became obvious with the detection of hundreds of point-sources in the Magellanic Clouds (MCs) at the detection limit of the *IRAS* satellite (e.g. Schwope 1989; Schwope & Israel 1989; Whitelock et al. 1989; Loup et al. 1997; Groenewegen & Blommaert 1998). These sources were then in part observed at other wavelengths mainly to identify the IR counterparts (Reid 1991; Zijlstra et al. 1996; van Loon et al. 1997), search for maser emission (Wood et al. 1992; van Loon et al. 2001; Marshall et al. 2004), monitor in the IR to obtain pulsation periods (Wood 1998; Whitelock et al. 2003), obtain near-IR spectra (van Loon et al. 1999a; Matsuura et al. 2005) and observed with the *Infrared Space Observatory* (*ISO*) satellite (Trams et al. 1999; Groenewegen et al. 2000). In addition, the *IRAS* result led to deeper surveys for AGB stars in the MCs with *ISO* in order to obtain less biased samples (Loup et al. 1999). More recently, the *Midcourse Space Experiment* (*MSX*) satellite mission also provided new AGB star candidates (Egan et al. 2001), some of which have already been observed spectroscopically in the near-IR (van Loon et al. 2006). Parallel to these developments on the observational side, there have been efforts in the modelling of these data by, e.g., Groenewegen & Blommaert (1998), van Loon et al. (1999b) and van Loon et al. (2005).

All these studies aimed at increasing our knowledge of the evolution on the AGB, in particular the evolution of mass loss and dust formation, also in the context of the difference in metallicity between our Galaxy, LMC and SMC. With the successful launch of the *Spitzer Space Telescope* (*SST*; Werner et al. 2004), fainter and more distant objects can be observed to study in more detail the dust formation process. In particular with the infrared spectrograph (IRS; Houck et al. 2004), high-quality spectra can be obtained of many individual objects in the MCs. The present paper aims to make detailed models of the IRS spectra and spectral energy distributions (SEDs) of carbon stars in the MCs in order to derive mass-loss rates.

In Section 2, the observational data are discussed, i.e. the *Spitzer* IRS spectra, light curves and periods from the literature and the

optical gravitational lensing experiment (OGLE) and massive compact halo object (*MACHO*) data bases, and the quasi-simultaneous ground-based *JHKL* photometry. Section 3 describes the radiative transfer models, and the results are presented in Section 4. The paper concludes with a discussion.

## 2 OBSERVATIONAL DATA

### 2.1 IRS spectra

Table 1 lists the sample of 60 carbon stars for which spectra have been obtained using the IRS onboard the *SST* using the low-resolution modules Short-Low (SL) and Long-Low (LL) between 5 and  $38 \mu\text{m}$  at a resolution of  $R = 68\text{--}128$ . The stars were observed as part of the General Observing time of *SST*, programmes 3505 (PI; P.R. Wood) and 3277 (PI; M. Egan).

Details of target selection, observations and data reduction as well as coordinates of the sources are described for programme 3505 in Zijlstra et al. (2006) for the LMC sources (IRAS 05132–6941 up to NGC 1978 IR4 in Table 1) and Lagadec et al. (2006) for the SMC sources (GM 780 up to IRAS 00554–7351 in Table 1), and for programme 3277 in Sloan et al. (2006) for the remaining SMC sources (MSX SMC 232 up to MSX SMC 033 in Table 1). Table 1 lists in the first column the identifier used in the present paper and alternative names in the second column.

### 2.2 Light curves and pulsation periods

The *MACHO*<sup>1</sup> and *OGLE*<sup>2</sup> data bases (Alcock et al. 1997; Zeburū et al. 2001) were searched in order to retrieve light curves and determine periods. For 36 objects, the light curves could be retrieved and they are shown in Fig. 1 in order of RA. For some objects, both *MACHO* and *OGLE* light curves are available. In that case, the *MACHO* *R* band was scaled and offset to fit the *OGLE* *I* band based on the data overlapping in time and the combined light curve is shown. Periods were determined by analysing the *MACHO* and combined *MACHO+OGLE* light curves in the way described by Groenewegen (2004, 2005), that is, using a combination of Fourier analysis and Phase Dispersion Minimization (PDM; see Stellingwerf 1978). For the stars with only an *OGLE* light curve, the period was directly taken from Groenewegen (2004). In some cases, the light curve is so irregular that no useful period can be derived, e.g. in the case of NGC 419 LE27/*OGLE* 010820.61-725251.7. In other cases, a Long Secondary Period (LSP; see e.g. Olivier & Wood 2003; Wood et al. 2004) is obvious, e.g. in LEGC 105/*OGLE* 005446.85-731337.6/*MACHO* 211.16247.8.

The dominant pulsation periods are listed in the third column in Table 1 together with other periods from the literature in the fourth column. The period quoted first is the adopted one and is used throughout this paper. Periods preceded by a star (★) indicate stars considered to have the most regular pulsation, and are identified as such in Figs 3–6. The last column lists the (semi-)amplitude of

<sup>1</sup> <http://www.macho.anu.edu.au/>

<sup>2</sup> <http://sirius.astro.uw.edu.pl/~ogle/>

**Table 1.** The carbon star sample: identifiers and pulsation periods.

Identifier	Other name(s)	Period	Ref.	Ampl. (filter)
IRAS 05132–6941	MSX LMC 223	*630	9	0.85 (K)
IRAS 05112–6755	TRM 4	830, 822	1, 7	0.88 (K)
IRAS 05190–6748	TRM 20	939, 889	1, 7	0.83 (K)
IRAS 05360–6648	MSX LMC 872; TRM 77	538, 530	1, 7	0.60 (K)
IRAS 05278–6942	MSX LMC 635	*980	9	1.20 (K)
IRAS 05295–7121	MSX LMC 692, MACHO 21.7768.2243	632, 682	pp, 1	0.71 (R)
IRAS 05113–6739	TRM 24	700, 713	1, 7	0.91 (K)
IRAS 04557–6753	–	765	1	0.68 (K)
IRAS 05009–6616	MSX LMC 1278	658	1	0.80 (K)
TRM 72	MSX LMC 29, MACHO 56.5052.258	556, 571, 631	pp, 1, 7	0.52 (R)
TRM 88	MSX LMC 310, MACHO 58.6508.122	*540, 544, 565	pp, 1, 7	1.02 (R)
MSX LMC 967	OGLE 053636.92-694722.3, MACHO 81.9122.1165	*537, 615	pp, 2	0.64 (J)
MSX LMC 749	OGLE 053527.04-695227.8, MACHO 81.8879.669	*540, 589	pp, 2	1.92 (J)
MSX LMC 349	–	*600	9	1.00 (K)
MSX LMC 754	MACHO 7.7779.1137	*462	pp	0.96 (R)
MSX LMC 743	–	*540	9	0.70 (K)
MSX LMC 441	–	*680	9	0.80 (K)
MSX LMC 679	–	*440	9	0.50 (K)
MSX LMC 443	–	*540	9	0.60 (K)
MSX LMC 601	OGLE 052650.96-693136.8	545	2	0.90 (J)
MSX LMC 494	OGLE 052309.18-691747.0, MACHO 80.6951.2338	*456, 458	pp, 2	0.92 (J)
MSX LMC 341	–	*580	9	0.75 (K)
MSX LMC 219	–	*670	9	1.05 (K)
GRRV 38	GRV 0529-6700; RGC 54, MACHO 60.7954.31	*503, 828	pp, 5	0.47 (R)
NGC 1978 MIR1	NGC 1978.8	*380	9	0.60 (K)
NGC 1978 IR1	NGC 1978.3, MACHO 64.7844.416	*431, 491	pp, 3	1.57 (R)
NGC 1978 IR4	NGC 1978.5, MACHO 64.7844.15	523	pp	0.18 (R)
GM 780	MACHO 213.15051.6	*608, 611	pp, 4	0.92 (R)
RAW 960	OGLE 005554.61-731136.3, MACHO 211.16305.35	*310, 296	pp, 2	0.43 (J)
NGC 419 MIR1	NGC 419.8	*700	9	0.75 (K)
NGC 419 LE35	NGC 419.7; OGLE 010817.45-725301.1, [GB98] S21	188	2	0.14 (J)
NGC 419 LE27	NGC 419.11; OGLE 010820.61-725251.7	–	pp	
NGC 419 LE18	NGC 419.17; OGLE 010824.89-725256.7	–	2	
NGC 419 LE16	NGC 419.1; OGLE 010801.10-725317.1	438	2	0.43 (J)
NGC 419 IR1	NGC 419.4; OGLE 010812.92-725243.7	453, 274, 526	pp, 2, 3	0.70 (J)
LEGC 105	OGLE 005446.85-731337.6, MACHO 211.16247.8	*346, 352	pp, 2	0.73 (J)
ISO 00548	OGLE 005450.73-730607.2, MACHO 211.16249.4703	*458, 440	pp, 2	1.13 (J)
ISO 01019	OGLE 010154.53-725822.1, MACHO 211.16707.28	*339, 334	pp, 2	1.05 (J)
ISO 00573	OGLE 005720.51-731245.8, MACHO 211.16419.244	*348, 354	pp, 2	0.57 (J)
ISO 00549	OGLE 005454.09-730318.0, MACHO 211.16250.4090	537, 524	pp, 2	0.48 (J)
IRAS 00554–7351	[GB98] S16	720	8	0.72 (K)
MSX SMC 232	OGLE 010603.28-722231.9, MACHO 206.17001.2488	508, –, 460	pp, 2, 6	0.65 (J)
MSX SMC 209	MACHO 207.16376.687	*521, 453, 520	pp, 4, 6	1.16 (R)
MSX SMC 202	–			
MSX SMC 200	–			
MSX SMC 198	OGLE 005710.97-723059.7, MACHO 207.16429.258	*543, 470, 500	pp, 2, 6	0.83 (J)
MSX SMC 163	MACHO 208.16031.578	*654, –, 660	pp, 4, 6	1.14 (R)
MSX SMC 162	OGLE 005240.16-724727.3, MACHO 207.16140.490	516, 529, 520	pp, 2, 6	0.39 (J)
MSX SMC 159	OGLE 005422.28-724329.7	540, 560	pp, 6	0.71 (J)
MSX SMC 142	OGLE 005140.46-725728.5, MACHO 212.16080.472	*296, 293, 300	pp, 2, 6	0.85 (J)
MSX SMC 105	OGLE 004502.14-725223.8, MACHO 208.15626.1306	*670, 689, 670	pp, 2, 6	0.71 (J)
MSX SMC 093	–			
MSX SMC 091	–			
MSX SMC 066	OGLE 004852.51-730856.5, MACHO 212.15907.28	492, 513, 530	pp, 2, 6	0.40 (J)
MSX SMC 062	OGLE 004240.89-725705.1, MACHO 213.15510.1225	*553, 491, 570	pp, 2, 6	0.96 (J)
MSX SMC 060	[GB98] S06, OGLE 004640.46-731646.9, MACHO 212.15734.3072	711, 350, –	8, 6, pp	0.52 (K)
MSX SMC 054	–			
MSX SMC 044	OGLE 004339.58-731457.1, MACHO 213.15563.34	*452, 461, 460	pp, 2, 6	0.55 (J)
MSX SMC 036	OGLE 004553.92-732340.7	548, 640	2, 6	0.90 (J)
MSX SMC 033	OGLE 004705.55-732132.5, MACHO 212.15789.1415	*540, 592, 530	pp, 2, 6	0.76 (J)

References: pp = present paper; 1 = Whitelock et al. (2003); 2 = Groenewegen (2004); 3 = Nishida et al. (2000); 4 = Raimondo et al. (2005); 5 = Reid et al. (1988); 6 = Sloan et al. (2006); 7 = Wood (1998); 8 = Dodion (2003); 9 = Wood et al. (in preparation). Periods preceded by a \* indicate stars considered to have the most regular pulsation (see Figs 3–6).

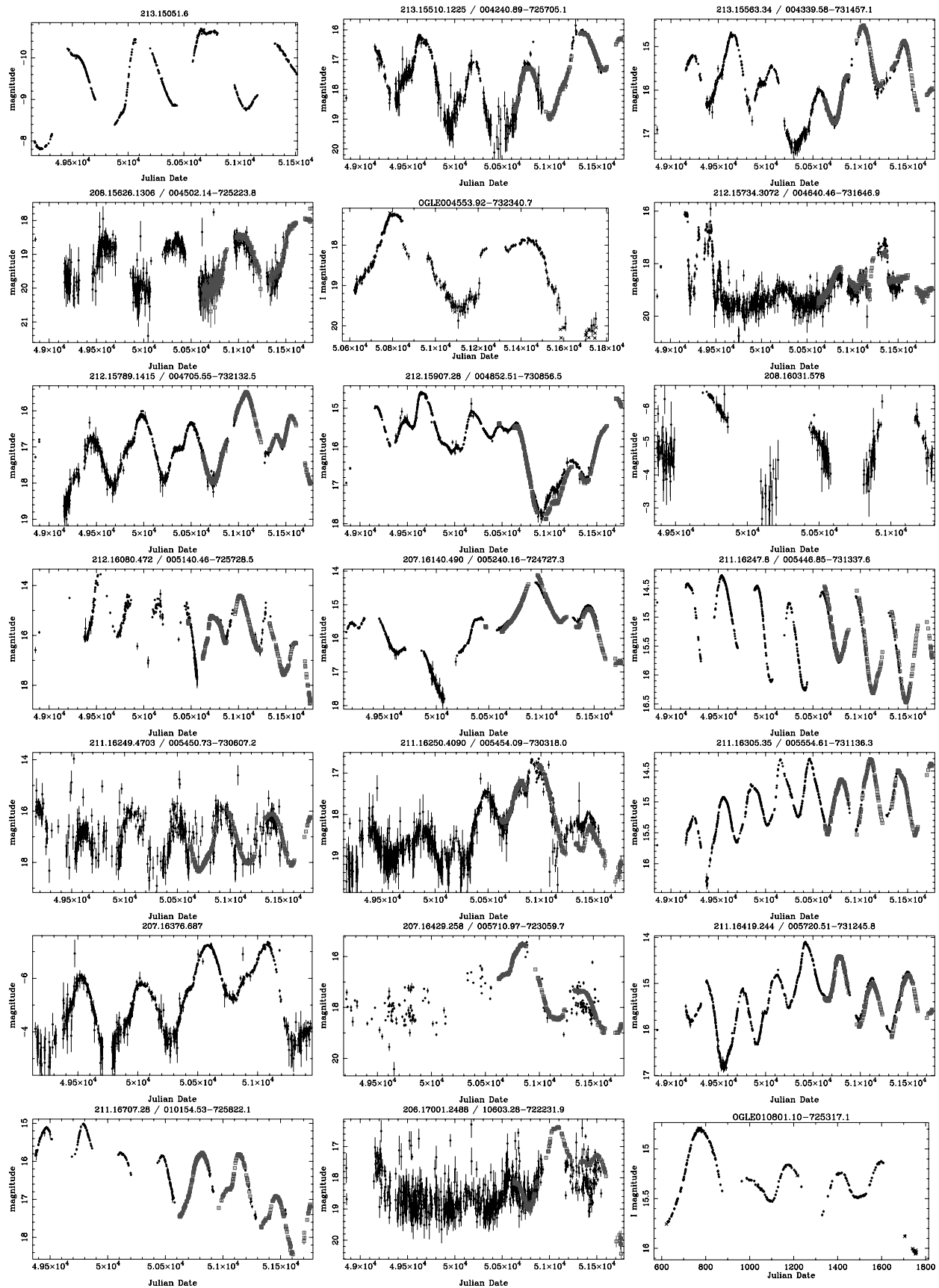


**Figure 1.** OGLE, MACHO and MACHO+OGLE light curves. In the last case, the instrumental MACHO *R*-band data (filled circles) have been scaled and offset to match the OGLE *I* band (open squares; coloured red in the electronic version). The MACHO and/or OGLE identity is given at the top of each plot. The abscissa is Julian Date – 2400 000.

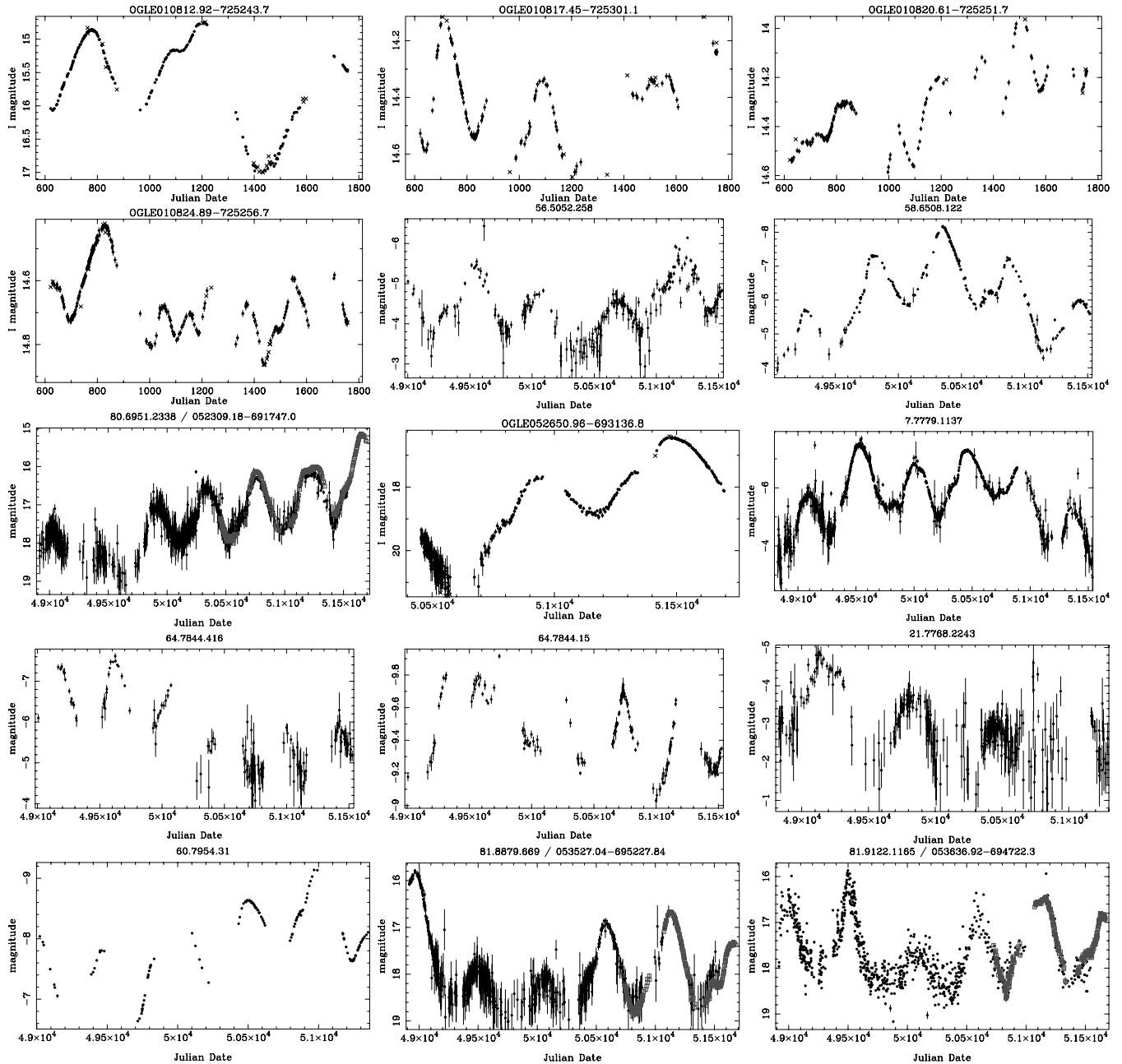


Figure 1 – continued

the adopted pulsation period in the filter where the light curve was obtained, i.e. OGLE *I*, MACHO *R* or *K*. The amplitudes are such that the observed (dominant) pulsation behaviour can be ascribed to Mira-like pulsation, except in the cases NGC 419 LE35 (*I* amplitude 0.14 mag).

The periods found here and in the literature are in reasonably good agreement with each other considering the irregular and non-periodic behaviour that is immediately obvious from inspecting the light curves in Fig. 1. Exceptions are as follows.

(i) GRRV 38 for which a (main) period of 503 d is found here (and a LSP of 3020 d) while Reid et al. (1988) quote 828 d based on an analysis of 23 photographic plates taken between 1976 Dec. and 1983 Feb. They do remark that in a *K*-band *PL*-diagram (their

fig. 8), it occupies an ‘anomalous position’, in the sense that for its *K*-band brightness, a period of 828 d is very long. Unfortunately, their individual data points are not published, so it cannot be verified how the data of 25 yr ago phase with the MACHO data and if the star actually changed period. In any case, its current main pulsation period is 503 d.

(ii) NGC 419 IR1 (OGLE 010812.92-725243.7) for which Groenewegen (2004) quote a period of 274 d based on OGLE data available at that time, which provided a bad fit though, and Nishida et al. (2000) who gave a period of  $526 \pm 18$  d based on IR monitoring. The currently available OGLE data were re-analysed to give a dominant period of 453 d and a secondary period of 977 d. There can be little doubt that the OGLE and IR observations refer to the same source. Based on the modelling of the SED, an *I*-band

magnitude of 16.1 is predicted well within the observed range during the OGLE observations of 15 to 17 mag. Using the program PERIOD98 (Sperl 1998) the *K*-band data by Nishida et al. have been independently analysed to find a period of 516 d (in good agreement with their value), and to derive a mean magnitude and amplitude. Then, these *K*-band data were transformed with  $[(K - 11.0) \times 1.6 + 15.6]$  to scale the amplitude and mean magnitude to that observed in the OGLE *I* band. A period analysis on this combined light curve (still dominated by the OGLE part) results in an unchanged period of 453 d, which is adopted here.

(iii) MSX SMC 060, for which Sloan et al. (2006) derive a period of 350 d based on a combination of MACHO and OGLE data, which cannot be confirmed in the present paper using the same data set as the light curve is too irregular. There exists, however, an IR light curve which has a clear period of 711 d (Dodion 2003).

### 2.3 Near-IR photometry

All of the stars in our sample were observed from the ground quasi-simultaneously with the *SST* observations. Ground-based observations were spaced at intervals of about 56 d, and linear interpolation between the two dates nearest the *SST* observation date was used to derive the *JHKL* values at that time.

The near-IR photometric observations were taken with the 2.3-m telescope at Siding Spring Observatory (SSO) in Australia, using the near-IR imaging system Cryogenic Array Spectrometer/Imager (CASPIR; McGregor et al. 1994) and the filters *J* (1.28  $\mu\text{m}$ ), *H* (1.68  $\mu\text{m}$ ), *K* (2.22  $\mu\text{m}$ ) and narrow-band *L* (3.59  $\mu\text{m}$ ). Standard stars from the lists by McGregor (1994) were used to calibrate the observations. Standard image reduction procedures of bias subtraction, linearization, bad pixel replacement, flat-fielding and sky subtraction were done with standard IRAF tasks. Aperture photometry was performed with the IRAF task QPHOT. All objects were observed twice and the photometry was averaged.

The photometry is listed in Table 2. For the sources MSX SMC 033 to 232, they have been published first by Sloan et al. (2006) but the data are repeated here for convenience and completeness. A full description of the IR monitoring program will follow in Wood et al. (in preparation).

## 3 THE MODEL

The dust radiative transfer model of Groenewegen (1993, also see Groenewegen 1995a) is used. This model was developed to handle non- $r^{-2}$  density distributions in spherically symmetric dust shells. It simultaneously solves the radiative transfer equation and the thermal balance equation for the dust.

When the input spectrum of the central source is fixed, the shape of the SED is exclusively determined by the dust optical depth, defined by

$$\begin{aligned} \tau_\lambda &= \int_{r_{\text{inner}}}^{r_{\text{outer}}} \pi a^2 Q_\lambda n_d(r) dr \\ &= 5.405 \times 10^8 \frac{\dot{M} \Psi Q_\lambda / a}{R_\star v_\infty \rho_d r_c} \int_1^{x_{\text{max}}} \frac{R(x)}{x^2 w(x)} dx, \end{aligned} \quad (1)$$

where  $x = r/r_c$ ,  $\dot{M}(r) = \dot{M}R(x)$  and  $v(r) = v_\infty w(x)$ . The normalized mass-loss rate profile  $R(x)$  and the normalized velocity law  $w(x)$  should obey  $R(1) = 1$  and  $w(\infty) = 1$ , respectively. In the case of a constant mass-loss rate and a constant velocity, the integral in equation (1) is essentially unity since  $x_{\text{max}}$  is typically much larger

than 1. The symbols and units in equation (1) are: the (present-day) mass-loss rate  $\dot{M}$  in  $M_\odot \text{yr}^{-1}$ ,  $\Psi$  the dust-to-gas mass ratio (assumed constant),  $Q_\lambda$  the extinction efficiency,  $a$  the grain size in cm (the model assumes a single grain size),  $R_\star$  the stellar radius in  $R_\odot$ ,  $v_\infty$  the terminal velocity of the dust in  $\text{km s}^{-1}$ ,  $\rho_d$  the dust grain specific density in  $\text{g cm}^{-3}$ ,  $r_c$  the inner dust radius in units of stellar radii and  $x_{\text{max}}$  the outer radius in units of  $r_c$ .

In the present model calculations, the outer radius is determined by a dust temperature of 20 K (which corresponds to a few 1000 times the inner radius, and ignores any possible heating by the ISM), a dust-to-gas ratio of  $\Psi = 0.005$ , a grain specific density typical for AMC of  $\rho_d = 2.0 \text{ g cm}^{-3}$ , a constant mass-loss rate, a constant outflow velocity of  $v_\infty = 10.0 \text{ km s}^{-1}$  and a velocity law of  $w = [0.01 + 0.99(1 - R_\star/r)^3]$  have been adopted. This law approximates the acceleration of the dust near the star. The LMC sources have been put at 50 kpc and the SMC sources at 61 kpc.

For the central star, the stellar atmosphere models by Loidl et al. (2001) have been used for  $T_{\text{eff}} = 2650$  (in the majority of cases), 2800, 3000 and 3200 K. Models with a carbon:oxygen (C/O) ratio of 1.4 have been preferred over the set of models with C/O = 1.1 as the C/O ratio is expected to be larger for a given stellar mass in the lower metallicity environment of the MCs. It is important to remark that these models have, except for carbon, solar elemental abundances and therefore are not appropriate for the stars in the MCs under consideration. Furthermore, these models are hydrostatic while, in principle, hydrodynamical models would be more appropriate in representing the stellar photosphere for these intrinsically pulsating stars. Notwithstanding these limitations, which must be kept in mind, it was felt that the hydrostatic solar-metallicity models of Loidl et al. are more appropriate than e.g. simple blackbodies.

For the dust species, a combination of AMC and SiC has been used, with optical constants from, respectively, Rouleau & Martin (1991) for the AC1 species and  $\alpha$ -SiC from Pégourié (1988). The extinction coefficients have been calculated in the small particle limit, and  $(Q_\lambda/a)$  is calculated from  $(Q_\lambda/a) = y (Q_\lambda/a)^{\text{SiC}} + (1-y) (Q_\lambda/a)^{\text{AMC}}$  where  $y$  is determined by the fit to the IRS spectrum.

The models have been corrected for a typical  $A_V = 0.15$  for all stars. The exact value is of no importance as this corresponds to  $\lesssim 0.02$  mag of reddening in the near-IR.

The free parameters of the model are the mass-loss rate, the luminosity, the effective temperature, the ratio  $y$  of SiC to AMC dust and the dust condensation temperature,  $T_c$ . For the latter, a default value of 1000 K for carbonaceous dust has been adopted. Only when the fits could significantly be improved, values as low as 860 K and as high as 1200 K have been tried.

The fitting procedure was as follows. For a given  $T_c$ , the dust optical depth was changed in order to fit the observed *J* – *K* colour (or *H* – *K* in case *J* was not available). Then, the luminosity was changed to fit the continuum in carbon stars at 6.4  $\mu\text{m}$  (see Zijlstra et al. 2006 for a discussion). If the fit to the IRS spectrum or the *H*, *L* photometry was poor, this procedure was repeated for different values of  $T_c$  and  $T_{\text{eff}}$ . The ratio of SiC to AMC dust is determined by the fit to the SiC feature in the IRS spectrum.

## 4 RESULTS

### 4.1 General

Table 3 contains the results of the model fitting: the luminosity, mass-loss rate, dust temperature at the inner radius, the mass ratio of SiC to AMC dust, the inner dust radius and the optical depth at the peak of the SiC feature at 11.33  $\mu\text{m}$ . The effective temperature

**Table 2.** The carbon star sample: quasi-simultaneous near-IR photometry.

Identifier	<i>J</i>	<i>H</i>	<i>K</i>	<i>L</i>
IRAS 05132–6941	–	15.409 ± 0.050	12.900 ± 0.026	9.596 ± 0.062
IRAS 05112–6755	–	15.228 ± 0.082	12.636 ± 0.026	9.274 ± 0.052
IRAS 05190–6748	–	17.265 ± 0.229	13.940 ± 0.047	9.829 ± 0.076
IRAS 05360–6648	–	16.307 ± 0.084	13.417 ± 0.038	9.980 ± 0.082
IRAS 05278–6942	–	15.229 ± 0.146	12.077 ± 0.022	8.380 ± 0.028
IRAS 05295–7121	17.250 ± 0.154	14.761 ± 0.044	12.391 ± 0.027	9.399 ± 0.069
IRAS 05113–6739	16.431 ± 0.110	14.162 ± 0.037	12.212 ± 0.020	9.516 ± 0.082
IRAS 04557–6753	17.607 ± 0.177	14.920 ± 0.039	12.676 ± 0.029	9.785 ± 0.072
IRAS 05009–6616	17.688 ± 0.307	14.806 ± 0.035	12.280 ± 0.037	9.127 ± 0.079
TRM 72	14.965 ± 0.028	12.997 ± 0.016	11.229 ± 0.018	8.771 ± 0.068
TRM 88	15.851 ± 0.079	13.628 ± 0.026	11.758 ± 0.023	9.282 ± 0.059
MSX LMC 967	13.457 ± 0.029	11.834 ± 0.025	10.412 ± 0.018	8.460 ± 0.048
MSX LMC 749	13.525 ± 0.033	11.614 ± 0.027	10.091 ± 0.019	8.176 ± 0.037
MSX LMC 349	–	16.299 ± 0.099	13.311 ± 0.034	9.762 ± 0.081
MSX LMC 754	13.973 ± 0.039	11.988 ± 0.030	10.643 ± 0.018	8.932 ± 0.036
MSX LMC 743	–	15.329 ± 0.054	12.815 ± 0.024	9.847 ± 0.131
MSX LMC 441	–	15.579 ± 0.084	13.108 ± 0.071	9.876 ± 0.072
MSX LMC 679	16.579 ± 0.134	14.224 ± 0.033	12.078 ± 0.022	9.277 ± 0.044
MSX LMC 443	–	15.114 ± 0.079	12.718 ± 0.035	9.794 ± 0.061
MSX LMC 601	15.865 ± 0.062	13.593 ± 0.031	11.709 ± 0.020	9.144 ± 0.057
MSX LMC 494	13.483 ± 0.028	11.708 ± 0.061	10.433 ± 0.019	8.925 ± 0.037
MSX LMC 341	–	15.265 ± 0.059	12.972 ± 0.029	9.718 ± 0.108
MSX LMC 219	–	15.943 ± 0.099	13.198 ± 0.050	9.909 ± 0.086
GRRV 38	12.086 ± 0.027	10.671 ± 0.022	9.751 ± 0.018	8.753 ± 0.059
NGC 1978 MIR1	–	14.389 ± 0.041	12.291 ± 0.020	9.590 ± 0.054
NGC 1978 IR1	14.146 ± 0.016	12.265 ± 0.013	10.747 ± 0.015	8.877 ± 0.060
NGC 1978 IR4	11.537 ± 0.012	10.308 ± 0.013	9.702 ± 0.015	9.250 ± 0.048
GM 780	12.980 ± 0.024	11.457 ± 0.023	10.225 ± 0.028	9.017 ± 0.039
RAW 960	13.391 ± 0.020	11.966 ± 0.037	10.958 ± 0.039	9.882 ± 0.103
NGC 419 MIR1	–	–	15.537 ± 0.131	11.472 ± 0.076
NGC 419 LE35	12.776 ± 0.014	11.574 ± 0.039	10.926 ± 0.035	10.288 ± 0.027
NGC 419 LE27	12.786 ± 0.021	11.658 ± 0.035	11.035 ± 0.034	10.496 ± 0.040
NGC 419 LE18	12.819 ± 0.016	11.662 ± 0.040	11.038 ± 0.035	10.218 ± 0.035
NGC 419 LE16	13.927 ± 0.014	12.469 ± 0.046	11.338 ± 0.035	10.026 ± 0.081
NGC 419 IR1	13.542 ± 0.019	11.953 ± 0.037	10.783 ± 0.033	9.109 ± 0.029
LEGC 105	14.334 ± 0.054	12.520 ± 0.024	11.248 ± 0.031	9.691 ± 0.108
ISO 00548	13.975 ± 0.060	12.389 ± 0.055	10.913 ± 0.027	9.163 ± 0.036
ISO 01019	13.154 ± 0.110	11.823 ± 0.044	10.922 ± 0.039	9.707 ± 0.054
ISO 00573	12.974 ± 0.035	11.674 ± 0.033	10.795 ± 0.033	9.783 ± 0.066
ISO 00549	14.698 ± 0.075	12.530 ± 0.025	11.029 ± 0.032	9.225 ± 0.058
IRAS 00554–7351	16.006 ± 0.091	13.439 ± 0.030	11.127 ± 0.033	8.458 ± 0.040
MSX SMC 232	15.539 ± 0.085	13.726 ± 0.042	12.029 ± 0.024	9.726 ± 0.286
MSX SMC 209	14.035 ± 0.025	12.147 ± 0.014	10.795 ± 0.007	8.908 ± 0.042
MSX SMC 202	12.974 ± 0.017	11.415 ± 0.013	10.423 ± 0.011	8.998 ± 0.044
MSX SMC 200	16.697 ± 0.086	14.182 ± 0.020	12.207 ± 0.025	9.736 ± 0.074
MSX SMC 198	14.659 ± 0.035	12.865 ± 0.016	11.442 ± 0.015	9.355 ± 0.099
MSX SMC 163	15.528 ± 0.044	13.280 ± 0.040	11.526 ± 0.023	9.266 ± 0.090
MSX SMC 162	13.850 ± 0.019	11.963 ± 0.025	10.575 ± 0.007	8.986 ± 0.113
MSX SMC 159	17.398 ± 0.199	15.010 ± 0.078	12.656 ± 0.017	9.534 ± 0.070
MSX SMC 142	14.129 ± 0.021	12.615 ± 0.036	11.404 ± 0.008	10.479 ± 0.227
MSX SMC 105	16.082 ± 0.129	13.687 ± 0.024	11.783 ± 0.009	9.540 ± 0.046
MSX SMC 093	13.053 ± 0.022	11.516 ± 0.034	10.403 ± 0.032	9.133 ± 0.080
MSX SMC 091	15.311 ± 0.077	13.334 ± 0.031	11.654 ± 0.011	9.917 ± 0.145
MSX SMC 066	13.305 ± 0.027	11.591 ± 0.013	10.263 ± 0.007	8.574 ± 0.058
MSX SMC 062	15.343 ± 0.033	13.235 ± 0.019	11.581 ± 0.009	9.501 ± 0.060
MSX SMC 060	15.011 ± 0.035	12.864 ± 0.016	11.048 ± 0.007	9.119 ± 0.052
MSX SMC 054	16.516 ± 0.325	14.326 ± 0.044	12.247 ± 0.012	9.841 ± 0.223
MSX SMC 044	15.579 ± 0.156	13.595 ± 0.025	11.806 ± 0.009	9.533 ± 0.087
MSX SMC 036	–	14.400 ± 0.024	12.711 ± 0.028	10.373 ± 0.095
MSX SMC 033	14.362 ± 0.022	12.404 ± 0.014	10.846 ± 0.008	8.775 ± 0.042

**Table 3.** Model results.

Identifier	Luminosity ( $L_{\odot}$ )	$\dot{M}$ ( $M_{\odot} \text{ yr}^{-1}$ )	$T_c$ (K)	SiC/AMC	$R_{\text{inner}}$ ( $R_{\text{star}}$ )	$\tau_{11.33 \mu\text{m}}$	Comment
GM 780	14100	1.2E-6	1150	8	5.19	0.266	$T_{\text{eff}} = 2800 \text{ K}$
GRRV 38	11900	6.6E-7	1200	2	6.18	0.102	$T_{\text{eff}} = 3200 \text{ K}$
IRAS 00554	26600	1.3E-5	1000	4	7.73	0.778	
IRAS 04557	7200	1.2E-5	860	2	11.08	0.719	
IRAS 05009	12900	9.4E-6	1070	4	6.89	0.957	
IRAS 05112	12400	1.8E-5	890	2	10.57	0.873	
IRAS 05113	9800	1.2E-5	800	2	12.57	0.525	
IRAS 05132	8300	9.5E-6	1000	2	8.04	0.818	
IRAS 05190	12800	2.3E-5	1000	2	8.93	1.377	
IRAS 05278	32400	2.5E-5	1000	2	8.39	1.025	
IRAS 05295	7900	9.0E-6	900	2	9.74	0.610	
IRAS 05360	6300	8.1E-6	1100	6	6.79	1.387	
ISO 00548	10500	2.2E-6	1000	2	6.70	0.220	
ISO 00549	9500	2.9E-6	1025	2	6.56	0.315	
ISO 00573	7900	6.2E-7	950	2	7.89	0.052	$T_{\text{eff}} = 2800 \text{ K}$
ISO 01019	7600	1.1E-6	900	2	10.70	0.071	$T_{\text{eff}} = 3000 \text{ K}$
LEGC 105	3900	1.1E-6	1050	2	5.95	0.179	
MSX LMC 219	5800	1.0E-5	950	2	9.11	0.865	
MSX LMC 341	6100	7.4E-6	1000	2	7.91	0.961	
MSX LMC 349	7700	8.0E-6	1100	2	6.67	1.190	
MSX LMC 441	7300	1.1E-5	950	2	9.06	1.080	
MSX LMC 443	5000	5.0E-6	1100	2	6.41	0.911	
MSX LMC 494	9300	1.4E-6	1075	2	5.56	0.200	
MSX LMC 601	6800	5.1E-6	930	2	8.64	0.361	
MSX LMC 679	8100	5.8E-6	1000	2	7.52	0.605	
MSX LMC 743	5000	7.4E-6	1000	2	8.02	1.041	
MSX LMC 749	18800	4.0E-6	1000	2	6.89	0.287	
MSX LMC 754	7800	1.7E-6	1100	2	5.44	0.299	
MSX LMC 967	14600	3.2E-6	950	2	7.60	0.225	
MSX SMC 033	16600	4.5E-6	1000	2	7.03	0.275	
MSX SMC 036	4000	3.5E-6	1000	2	7.39	0.490	
MSX SMC 044	7900	4.0E-6	950	2	8.00	0.293	
MSX SMC 054	6000	3.6E-6	1000	2	7.24	0.424	
MSX SMC 060	12500	5.6E-6	950	2	8.09	0.321	
MSX SMC 062	6400	3.2E-6	1000	2	7.13	0.308	
MSX SMC 066	16300	3.4E-6	1000	2	6.84	0.218	
MSX SMC 091	4400	1.5E-6	1075	2	5.80	0.291	
MSX SMC 093	7900	5.0E-7	1200	2	4.09	0.134	
MSX SMC 105	8100	4.3E-6	1100	2	5.72	0.355	
MSX SMC 142	4800	5.4E-7	1200	2	4.20	0.145	
MSX SMC 159	5300	4.8E-6	1000	2	7.54	0.667	
MSX SMC 162	10400	1.3E-6	1200	2	4.40	0.264	
MSX SMC 163	10200	3.3E-6	1075	2	6.03	0.429	
MSX SMC 198	7200	1.5E-6	1075	2	5.67	0.194	
MSX SMC 200	5400	2.6E-6	1200	2	5.00	0.479	
MSX SMC 202	11900	8.8E-7	1100	2	5.07	0.107	
MSX SMC 209	13800	3.6E-6	950	2	7.71	0.210	
MSX SMC 232	5600	2.9E-6	950	2	7.88	0.258	
NGC 1978 IR1	9000	2.3E-6	1050	2	6.12	0.286	
NGC 1978 IR4	15700	2.2E-7	1000	2	5.99	0.021	
NGC 1978 MIR1	6900	6.2E-6	1000	2	7.67	0.681	
NGC 419 IR1	12200	2.0E-6	1000	2	8.57	0.137	$T_{\text{eff}} = 3000 \text{ K}$
NGC 419 LE16	5000	5.1E-7	1200	2	5.38	0.111	$T_{\text{eff}} = 3000 \text{ K}$
NGC 419 LE18	7200	2.2E-7	1100	2	7.34	0.028	$T_{\text{eff}} = 3200 \text{ K}$
NGC 419 LE27	6800	1.0E-7	1075	2	6.51	0.017	$T_{\text{eff}} = 3000 \text{ K}$
NGC 419 LE35	7000	1.1E-7	1200	2	4.98	0.023	$T_{\text{eff}} = 3000 \text{ K}$
NGC 419 MIR1	5000	1.7E-5	1000	2	9.19	1.566	
RAW 960	6100	3.5E-7	1200	2	4.03	0.110	
TRM 72	13000	5.8E-6	1000	2	7.31	0.457	
TRM 88	6400	3.3E-6	1025	0	6.82	0.339	

of the adopted model atmosphere is 2650 K except when noted in the last column. The coolest of the available model atmospheres is adopted as the default as this appears to be the most appropriate choice for carbon stars at the tip of the AGB (e.g. Marigo 2002). In the optically thick case, the effect of  $T_{\text{eff}}$  on the emerging spectrum is small. Approximate  $1\sigma$  error bars are of the order of 20 per cent in the luminosity, about 50 K in the condensation temperature and about 10 per cent in the optical depth (and hence the mass-loss rate for a given luminosity, effective temperature and condensation temperature).

To give an absolute error estimate on the mass-loss rate is very difficult as it involves the uncertainties mentioned above (in  $T_{\text{eff}}$  and  $T_c$ ), as well as uncertainties in the dust optical properties, the dust-to-gas ratio, expansion velocity, the assumption of spherical symmetry and the exact acceleration of the dust near the star. A factor of 2 uncertainty in the mass-loss rate in the optically thick models and a factor of 3 in the optically thin models are realistic.

Fig. 2 displays the model fits to the data. In the top panels, the fit to the IRS spectrum and the NIR photometry is shown on a logarithmic scale; in the bottom panels the fit to the IRS spectrum is shown on a linear scale. Only in the case of the stars in the clusters NGC 419 and 1978 is additional mid-IR photometry from *ISO* plotted (Tanabé et al. 2004) as an additional check that the observed IRS spectrum refers to the intended target and that there were no problems with the peak-up of IRS (cf. Lagadec et al. 2006).

As only AMC and SiC are included in the model to describe the dust components, it is understandable that the dust complex around 28  $\mu\text{m}$  is not fitted. This complex is commonly attributed to magnesium-sulphide (MgS) dust grains (e.g. Goebel & Moseley 1985). Inspection of Fig. 2 illustrates the large variety of MgS features from essentially absent (e.g. IRAS 05132) to strong (e.g. IRAS 05360). A more detailed description of the MgS feature in the present sample can be found in Sloan et al. (2006) and Zijlstra et al. (2006). Hony & Bouwman (2004) showed that the emission feature shifts to longer wavelength with decreasing grain temperature, and that therefore a temperature and a corresponding distance to the star can be inferred from the observed MgS profile. Such a study is beyond the scope of the present paper however.

On inspecting Fig. 2, it also becomes clear that the feature near 7.5  $\mu\text{m}$ , which is attributed to  $\text{C}_2\text{H}_2$  (see e.g. Matsuura et al. 2006), is not well represented in the adopted model atmospheres.

In general, the quality of the fits to the SEDs and IRS spectra is high. The lowest quality is generally obtained when the mass-loss rate is low (e.g. GRRV 38, GM 780, RAW 960, NGC 1978 IR1, LEGC 105). This is most likely due to the limitations in the model atmospheres used. In these cases, prominent molecular absorption is present which is discussed in more detail in Sloan et al. (2006), Zijlstra et al. (2006), Matsuura et al. (2006) and Lagadec et al. (2006) for the present sample.

In a few cases, the data of stars which clearly have substantial mass loss cannot be fitted satisfactorily (e.g. MSX SMC 033, 044, 060, but see Section 5.4 for a possible explanation). There could be an undetected problem in the data reduction (although the data reduction was done independently by two of us for these three sources), or one of the assumptions in the modelling no longer holds, e.g. the assumption of spherical symmetry.

## 4.2 Mass loss and luminosity

Fig. 3 shows the mass-loss rate for the SMC (squares) and LMC (triangles) plotted as a function of luminosity. Also indicated is whether the star shows Mira-like pulsation amplitudes (open symbols; see

discussion in Section 2.2) or not, or if there is no information available (filled symbols). In the bottom panel, the stars without pulsation information available (plus signs) or the ones with non-regular pulsation (cross signs) have been marked. The solid line is the relation derived by Groenewegen et al. (1998) for 44 Galactic carbon Miras with (mean) luminosities between 4400 and 16 400  $L_\odot$ . The dashed and dot-dashed lines come from van Loon et al. (1999b) and represent, respectively, the empirical observed maximum ( $\propto L$ ), and the classical limit [ $\propto L/(c v_{\text{exp}}) \propto L^{0.75}$ ], to the mass-loss rate observed in a sample of 57 mass-losing AGB and RSG stars in the LMC.

Several observations may be made. It seems that all stars remain clearly below the maximum mass-loss limit proposed by van Loon et al., and in fact the classical single scattering limit seems to mark the maximum mass-loss rate observed in the present sample. The line of maximum mass loss was based on six oxygen-rich stars with  $\log L \gtrsim 4.3$  and one carbon star which had  $\log L = 3.55$  and  $\log \dot{M} = -4.4$ . Unfortunately, this star (IRAS 05289–6617, a.k.a. TRM 99) is not in the present sample as no IRS spectrum has been taken.

A difference between the present study and those of Groenewegen et al. and van Loon et al. is that here the expansion velocity for both SMC and LMC sources is assumed to be 10  $\text{km s}^{-1}$ . In Groenewegen et al., the expansion velocity of the Galactic carbon Miras was available for almost all sources from CO molecular line emission data. There is a considerable scatter, but on average the expansion velocity in Galactic carbon Miras increases from  $\sim 8 \text{ km s}^{-1}$  at 5000  $L_\odot$  to  $\sim 25 \text{ km s}^{-1}$  at 12 000  $L_\odot$  (and with very few data points available at higher luminosities). In van Loon et al., the expansion velocity was available for some of the oxygen-rich sources from OH maser emission, and in other cases was estimated from  $v_{\text{exp}} = 10 (L/30\,000)^{0.25} \text{ km s}^{-1}$ , which implies a range from 6.0 to 10.2  $\text{km s}^{-1}$  for the carbon stars in the present sample which have luminosities ranging from 3900 to 32 400  $L_\odot$ . Adopting such an approach would have a small effect on the appearance of Fig. 3. The mass-loss rate of the brightest sources would remain essentially unchanged while that of the least luminous sources would decrease by a factor of 10/6 (see equation 1), or the equivalent of one tick mark in the figure.

At a given luminosity, the mass-loss rate of the LMC objects appears to be larger by about a factor of 3 than those of the SMC objects. This is definitely true for the dust mass-loss rate, but the conversion to total mass-loss rate assumes a constant dust-to-gas ratio (0.005) and expansion velocity (10  $\text{km s}^{-1}$ ). In the Galaxy, a dust-to-gas ratio was derived which depends on luminosity, rising from  $\sim 0.003$  at  $\log L = 3.7$  to  $\sim 0.01$  at  $\log L = 4.1$  (Groenewegen et al. 1998). In the Galaxy, its effect on the mass-loss rate is compensated for by a similar change in expansion velocity with luminosity, as mentioned above.

One may also note that the data points do not fit the mean relation derived for Galactic Miras. If the observed higher mass-loss rate for LMC objects compared to SMC ones is real and due to a metallicity effect, one might have expected the LMC data points to cluster around or below the mean line for Galactic C-stars as well. One way to lower the LMC mass-loss rates would be to adopt a dust-to-gas ratio larger than 0.005, or an expansion velocity lower than 10  $\text{km s}^{-1}$ . Both options seem not very likely, as one expects the dust-to-gas ratio to be lower in a low-metallicity environment, and the adopted expansion velocity is already lower than observed in the Galactic ones.

One may also notice a considerable scatter in Fig. 3. This is in part real and due to differences between the stars in terms of stellar temperature (evolution) and initial metallicity, and hence dust-to-gas

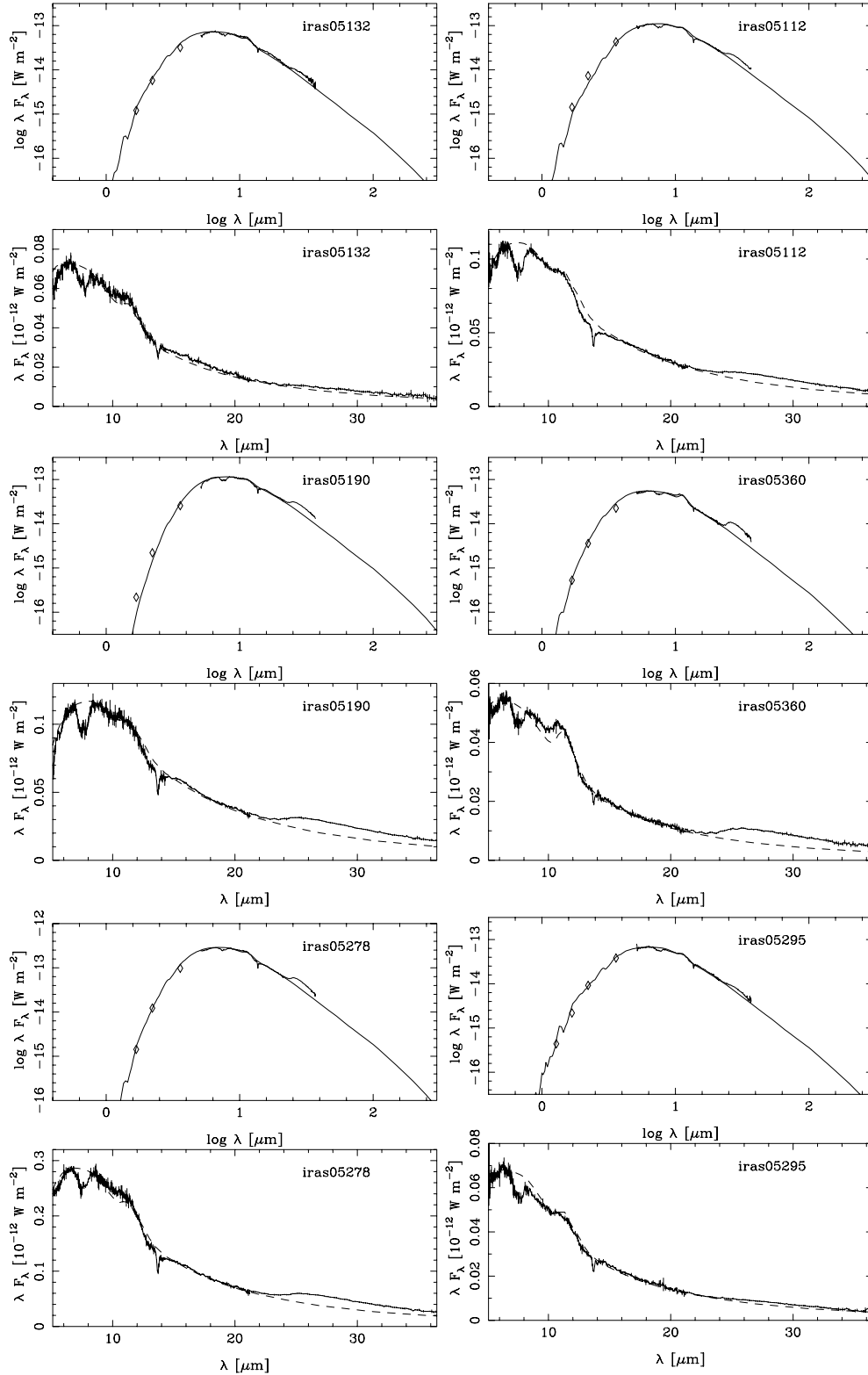


**Figure 2.** Fits to the SED in the top panel, and the IRS spectrum in the bottom panel.

ratio [e.g. van Loon et al. (2005) quantified the temperature effect in a sample of oxygen-rich objects]. The scatter is also in part due to the fact that the data have been analysed as a single epoch. Changing  $L$  by 1 mag has an effect of 0.2 dex on the derived mass-loss rate

with all other parameters being equal, as indicated by the arrow in Fig. 3. In Groenewegen et al., the period was used with a  $PL$ -relation to obtain the (mean) luminosity and from that derive the distance and the mass-loss rate.

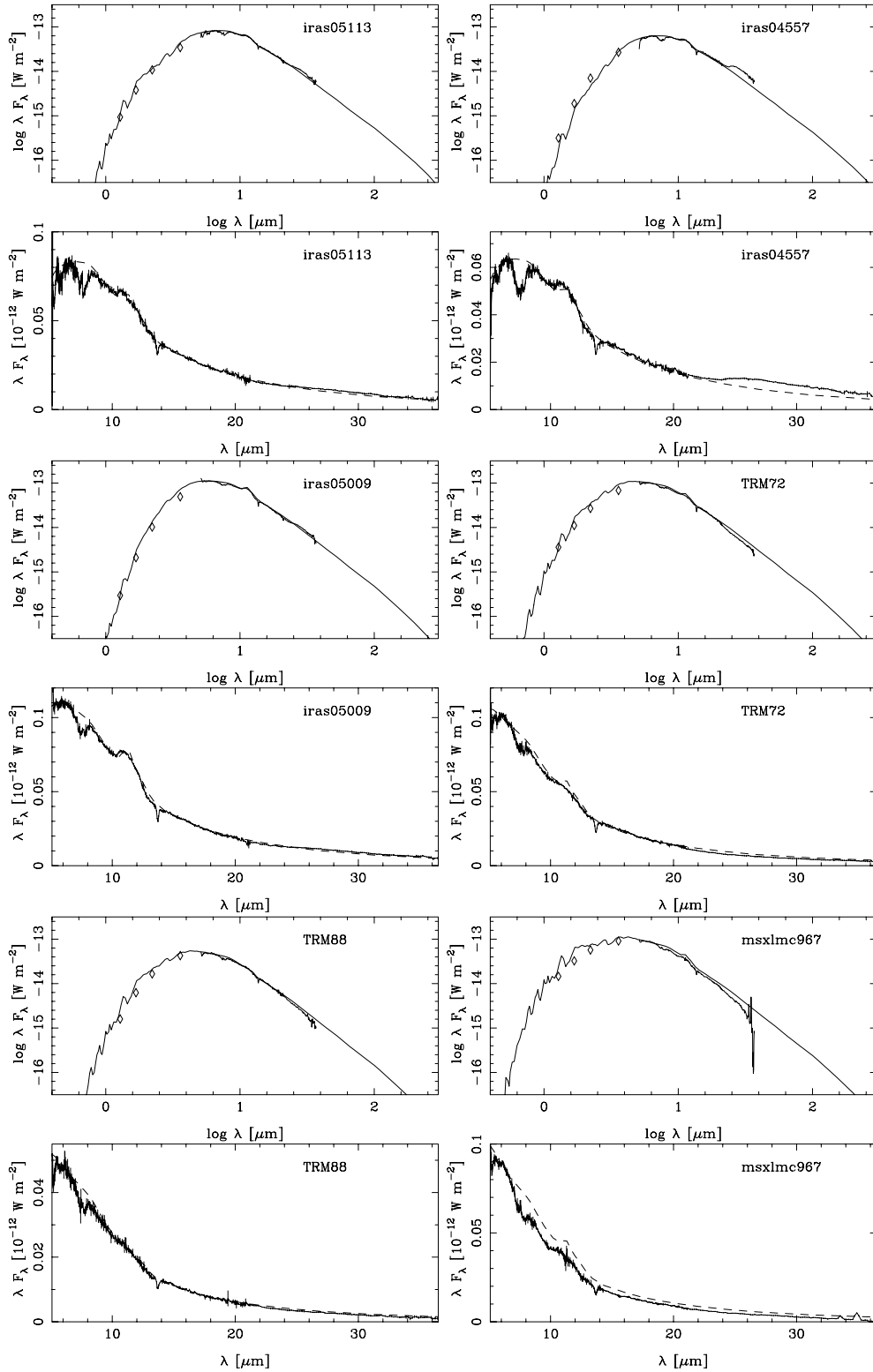
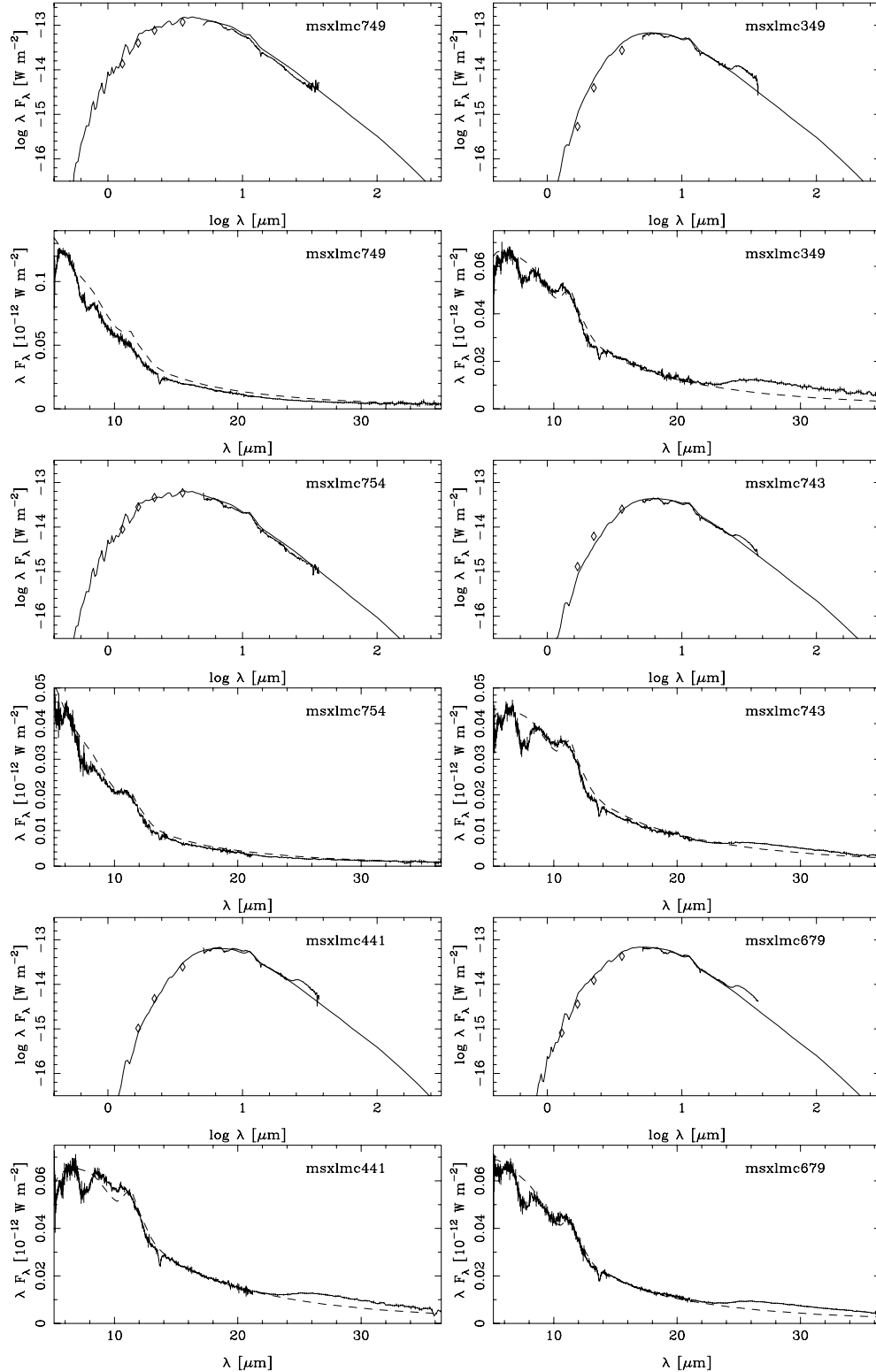


Figure 2 – continued

### 4.3 Mass loss and pulsation period

Fig. 4 shows the mass-loss rate as a function of pulsation period. Symbols in the upper and lower panel have the same meaning as in Fig. 3. The solid line is a fit from Groenewegen et al. (1998) de-

rived from Galactic carbon Miras. The situation seems much clearer than in the previous figure. There is much less scatter and LMC, SMC and Galactic Miras seem to follow *the same* trend of increasing mass-loss rate with increasing pulsation period. This apparent contradiction may be related to the fact that the pulsation period

Figure 2 – *continued*

is related to stellar properties averaged over the  $\sim 300\text{--}1000$  d of a pulsation cycle, while the luminosity is an instantaneous value measured at a random phase of the pulsation cycle. Keeping the slope derived by Groenewegen et al. (1998) for Galactic C-rich Miras ( $d \log \dot{M} / d \log P = 4.08$ ), a linear fit was made to the mass-loss

rates to derive a zero point of  $-16.60 \pm 0.32$  for the SMC sources (excluding the outlier NGC 418 IR4) and  $-16.51 \pm 0.17$  for the LMC sources, compared to  $-16.54 \pm 0.27$  for the Galactic sources in Groenewegen et al. (1998). Based on this, one concludes that at a given period, Galactic, SMC and LMC Miras have very similar

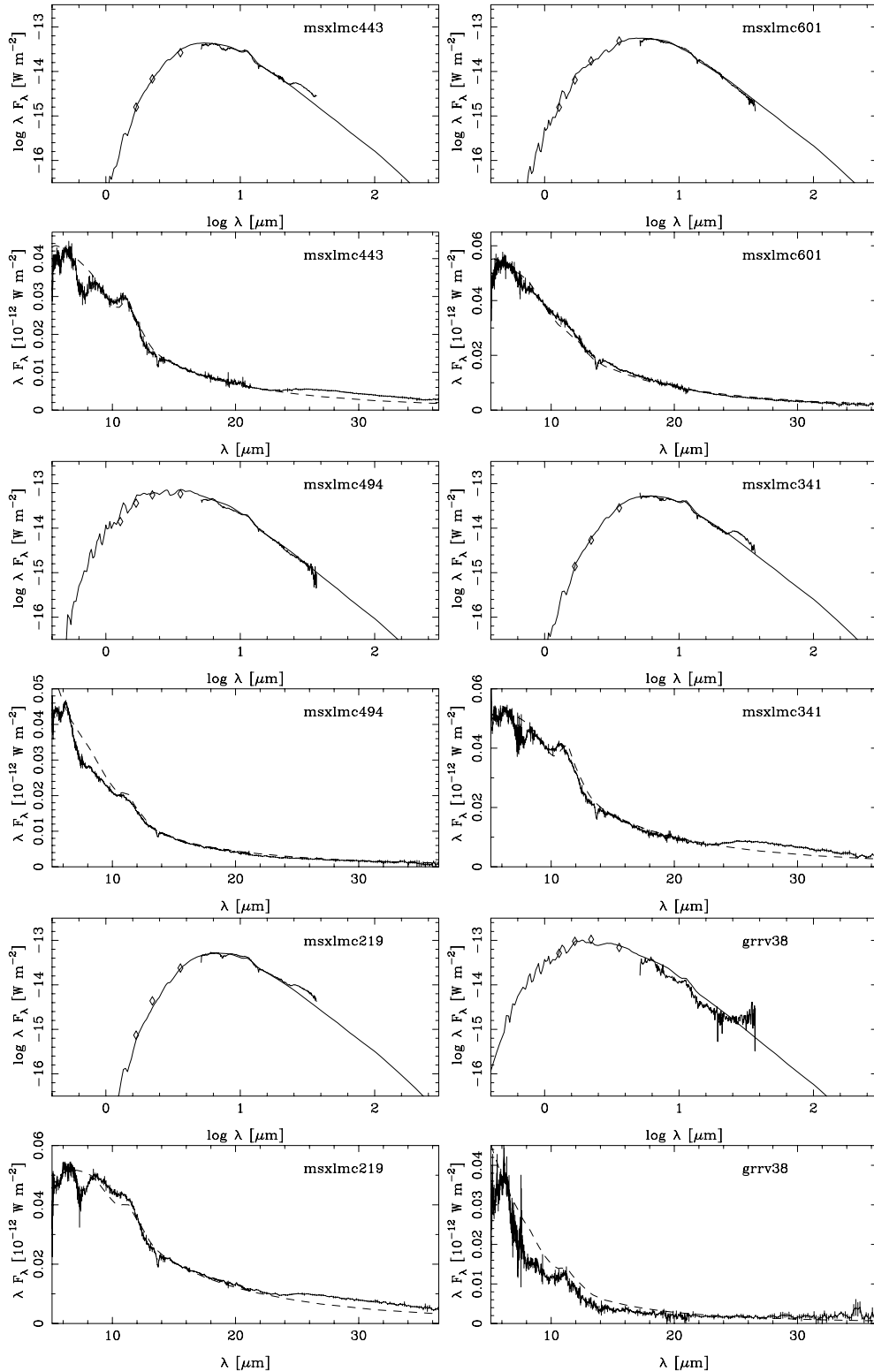


Figure 2 – continued

mass-loss rates. (The remarks about the effect of the adopted dust-to-gas ratio and expansion velocity on mass-loss rate do apply here as well however.) The dispersion in the LMC sample is smaller than that in the Galactic and SMC sample, but if this is significant is unclear.

#### 4.4 Luminosity and pulsation period

Fig. 5 shows the bolometric luminosity plotted against period. Symbols in the upper and lower panel have the same meaning as in Fig. 3. The solid line is an extrapolation of the  $PL$ -relation derived by Feast

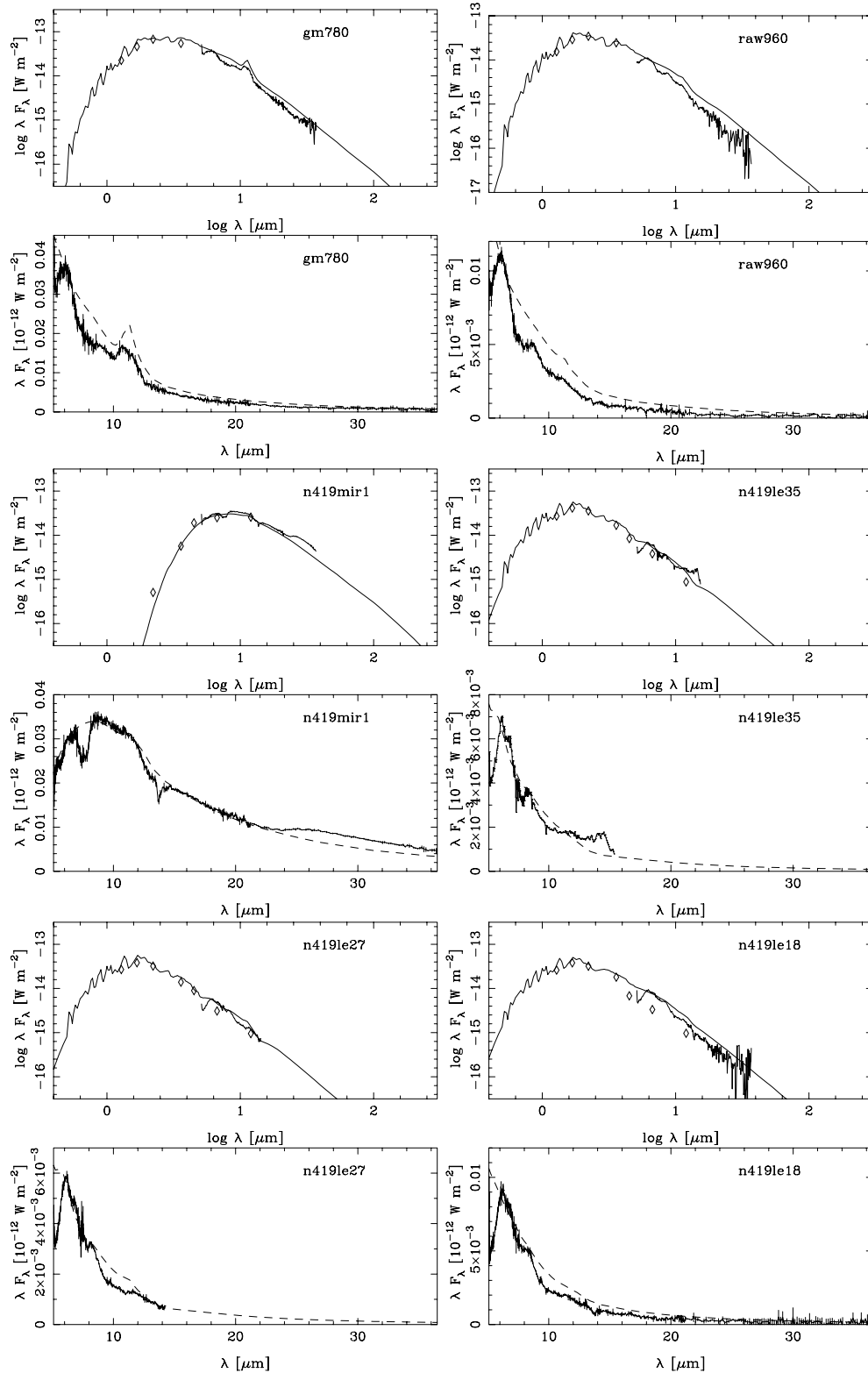


Figure 2 – continued

et al. (1989) for carbon Miras with periods below 420 d, assuming an LMC distance of 50 kpc, while the dashed line is the more recent C-star *PL*-relation based on LMC stars with periods up to 900 d from Whitelock et al. (2006). The dot-dashed line represents the *PL*-relation below and above 450 d derived by Hughes & Wood

(1990) for (mainly O-rich) Mira and Semi-Regular variables in the LMC.

In both the panels, there is considerable scatter at a given period. Part of this could be due to the variation of the luminosity over the pulsation cycle. For six stars in common with Whitelock et al.

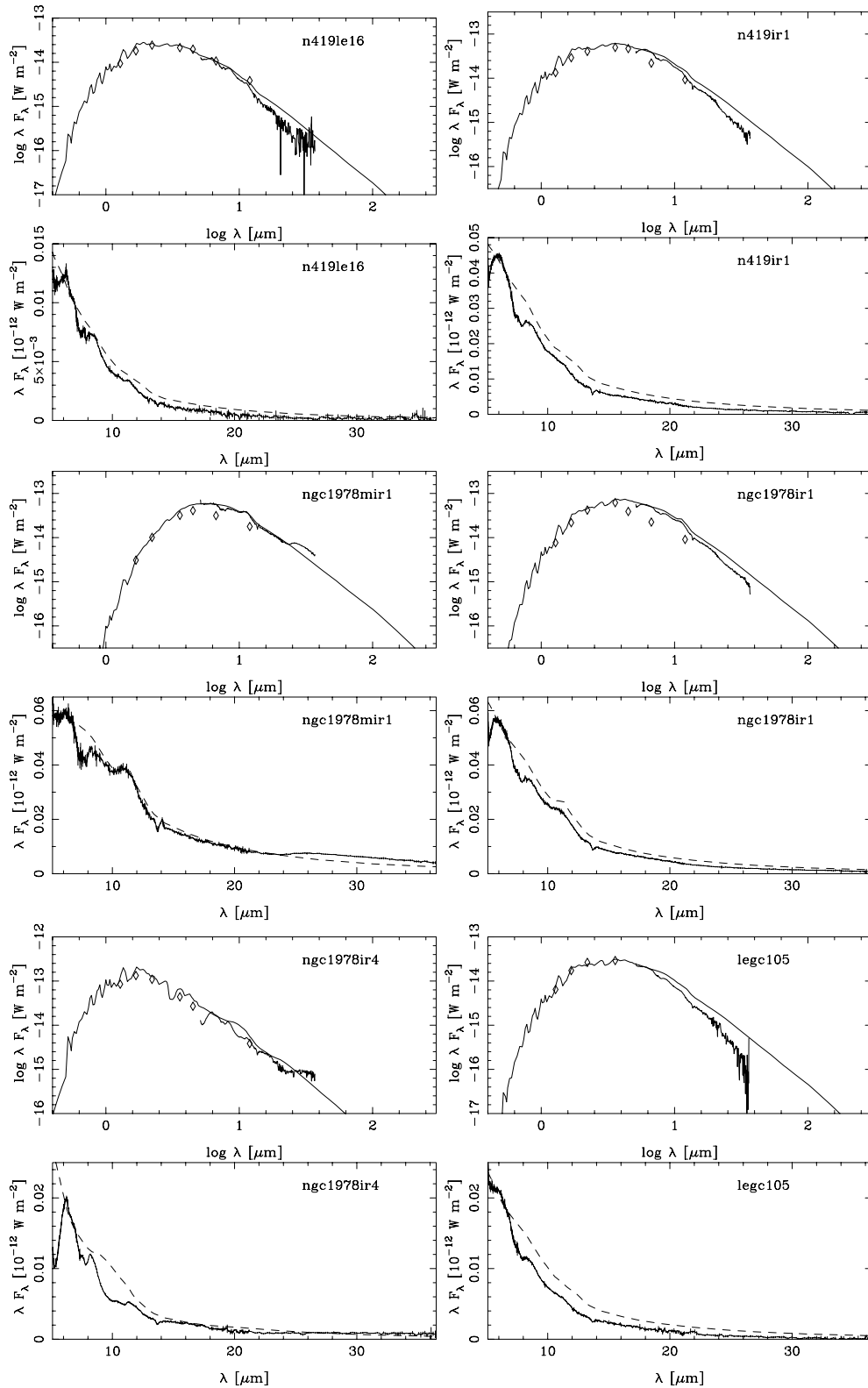


Figure 2 – continued

(2006), the difference between our single-epoch and their intensity-averaged luminosity ranges from  $-0.41$  to  $+0.34$  mag in  $M_{\text{bol}}$ .

Most of the stars showing regular pulsation seem to cluster around the  $PL$ -relation either by Hughes & Wood (1990) or by Whitelock

et al. (2006), while most of the stars showing non-regular pulsation appear to scatter around the  $PL$ -relation by Whitelock et al.

Fig. 6 shows the estimated  $K$ -band magnitude plotted against period. Symbols in the upper and lower panel have the same meaning

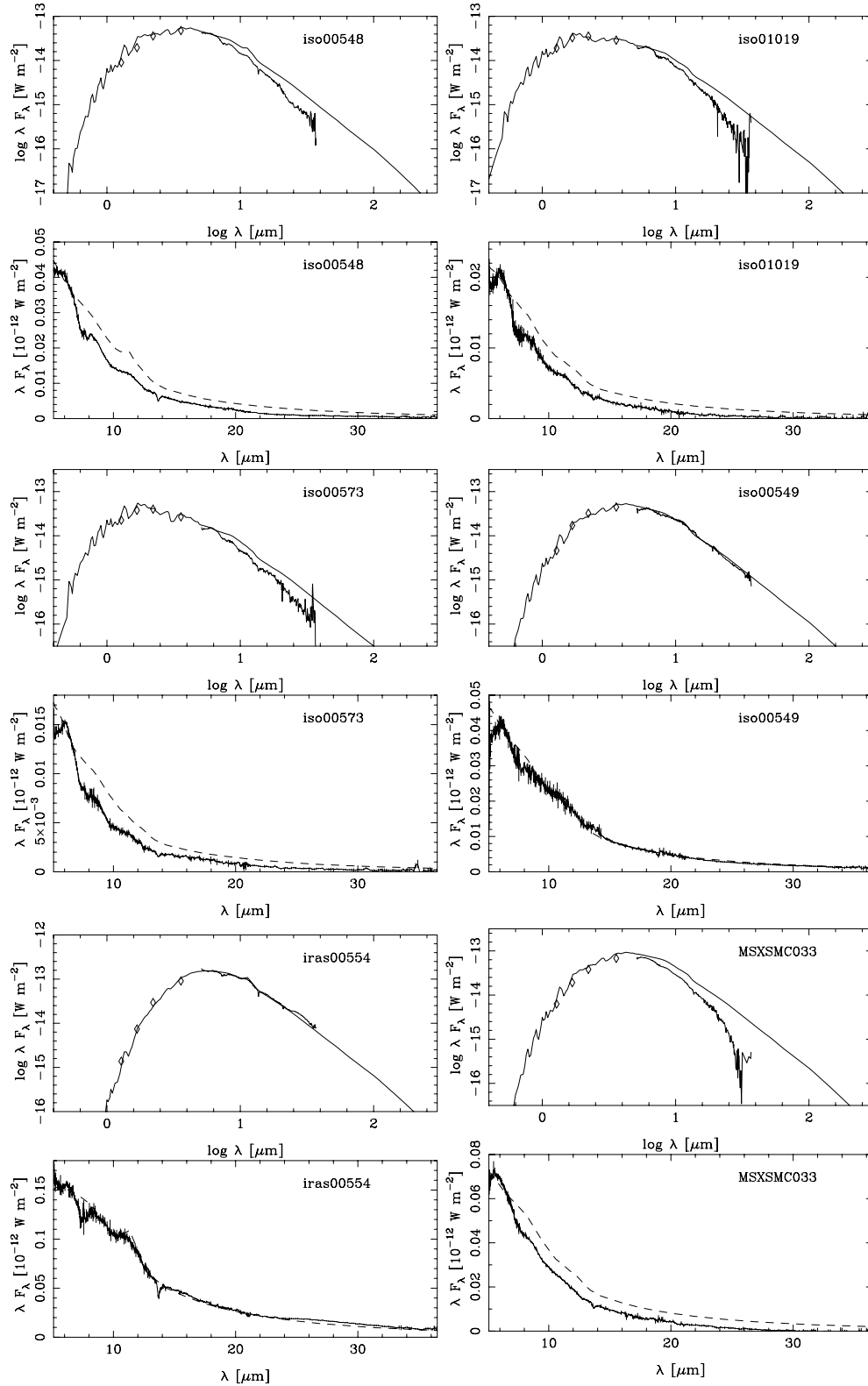


Figure 2 – continued

as in Fig. 3. Here, since the *K*-band magnitude will be dimmed by dust obscuration the models have been re-run for zero mass-loss rate, and the 2MASS *K* magnitude has been determined. In other words, we are simply using a luminosity-scaled version of the Loidl et al.

stellar spectra to compute the *K* magnitude. The solid line in Fig. 6 is the *K*-band *PL*-relation from Groenewegen & Whitlock (1996) for stars up to periods of 500 d, while the dashed region corresponds to box ‘C’ in Groenewegen (2004), defining the location of the

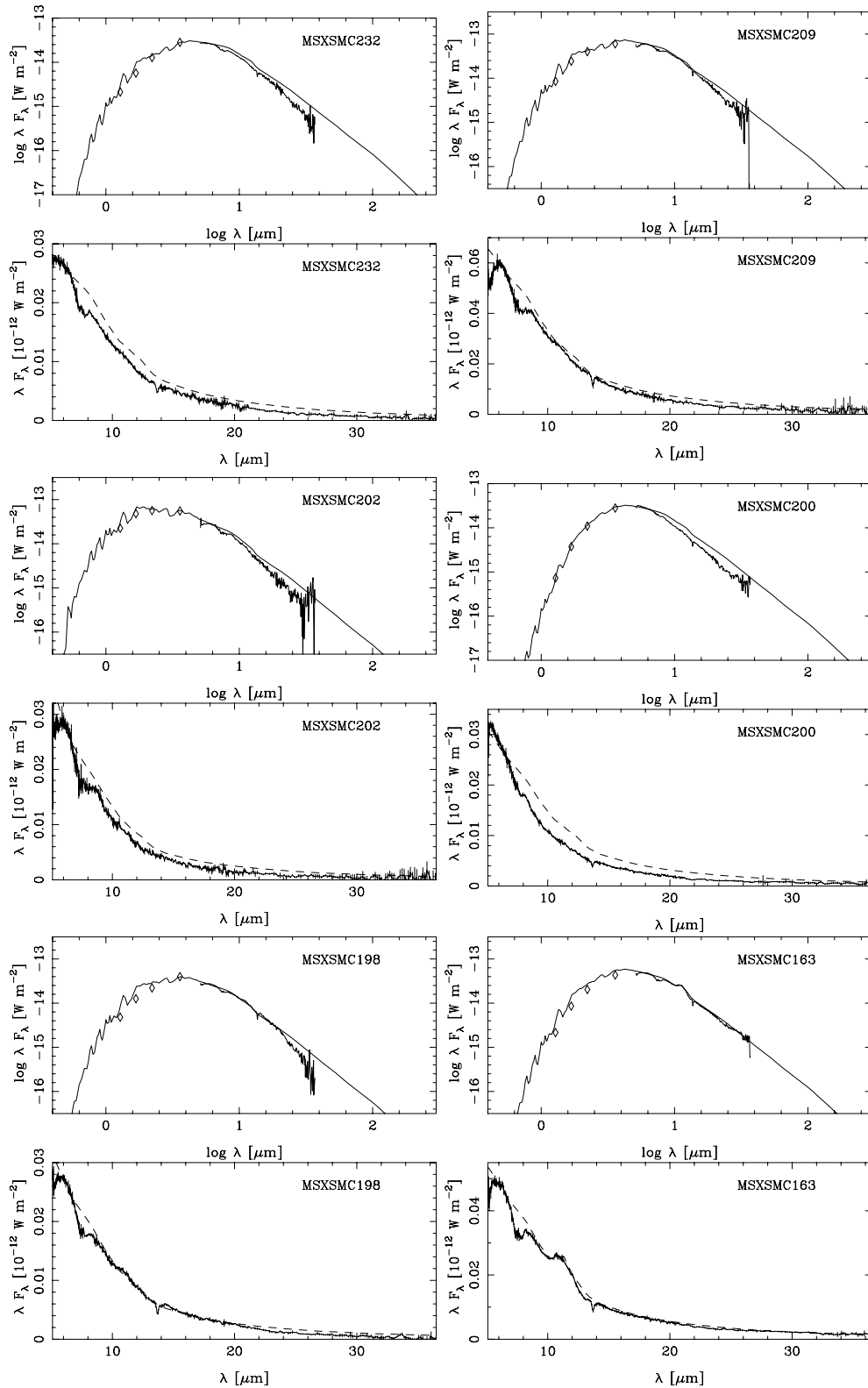
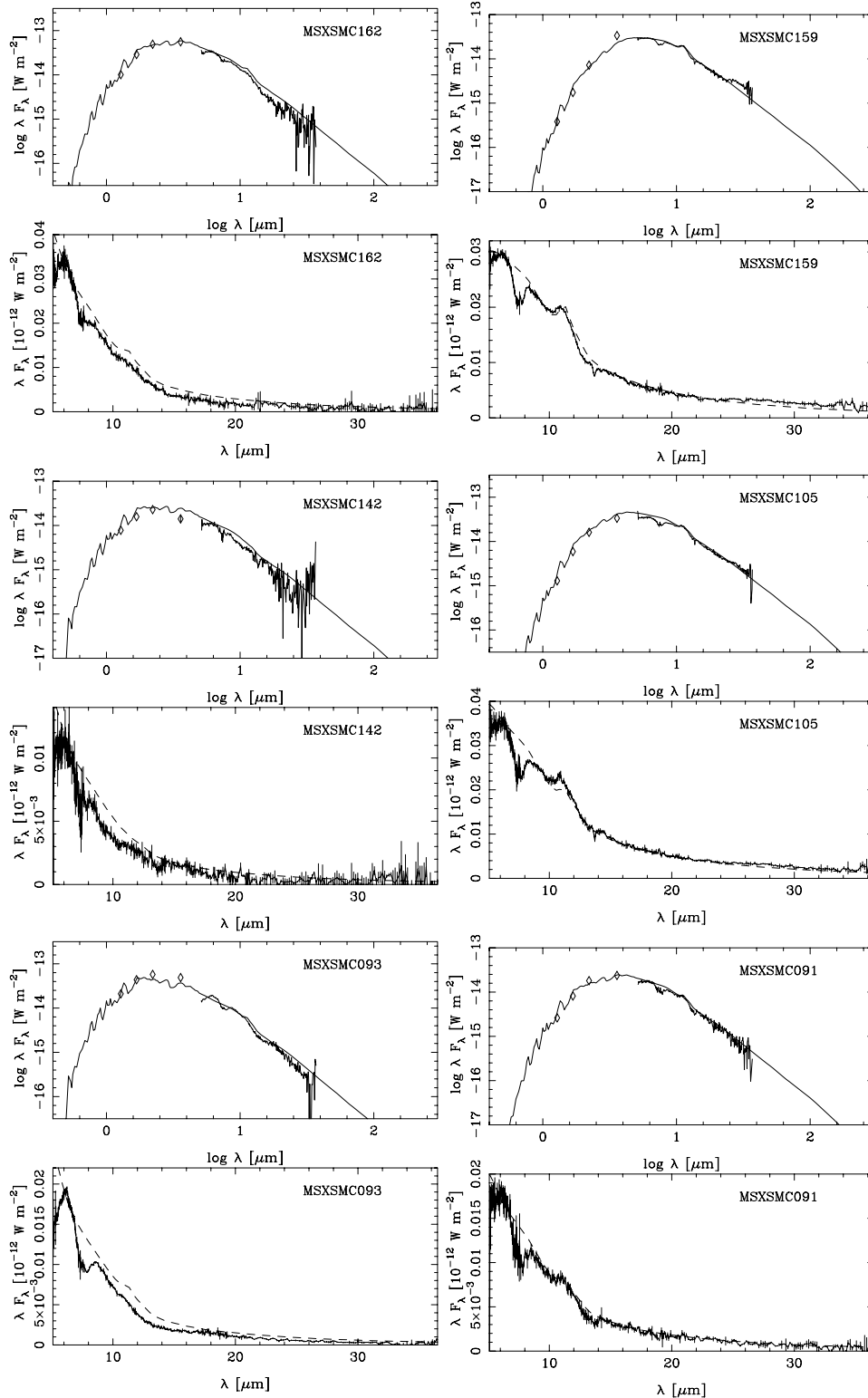


Figure 2 – continued

large-amplitude variables. The large majority of stars are indeed located inside box ‘C’, especially the most regular pulsators. As for the plots with luminosity as one of the parameters on the axis, the effect of single-epoch data versus average over the pulsation cycle

must be kept in mind. The peak-to-peak amplitude of Mira variables is at least 0.4 mag in *K*. With this in mind, one can conclude that the location of all large-amplitude variables (the open symbols) is consistent with the location of box ‘C’.

Figure 2 – *continued*

## 5 DISCUSSION

### 5.1 The ‘Manchester method’

Sloan et al. (2006), Zijlstra et al. (2006) and Lagadec et al. (2006) have used what they describe as the ‘Manchester method’ to analyse

the IR spectra of carbon stars. A key assumption they have made is that the colour derived from narrow photometric bands centred at 6.4 and 9.3  $\mu\text{m}$  can serve as a proxy for the mass-loss rate from the star. These bands were chosen to avoid obvious molecular bands, and the [6.4]–[9.3]  $\mu\text{m}$  colour is measured directly from the spectrum over the wavelength ranges 6.25–6.55 and 9.10–9.50  $\mu\text{m}$ .

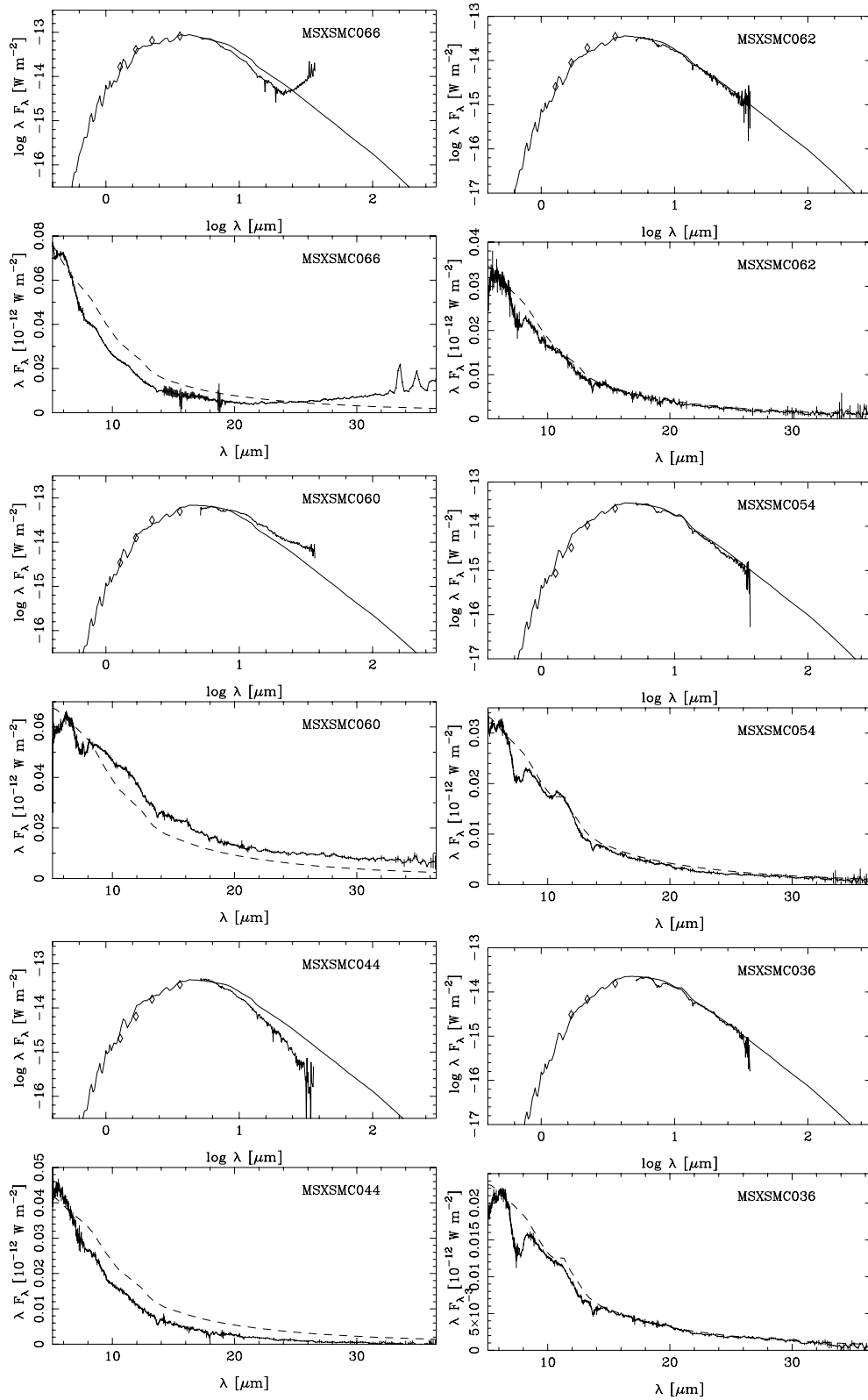
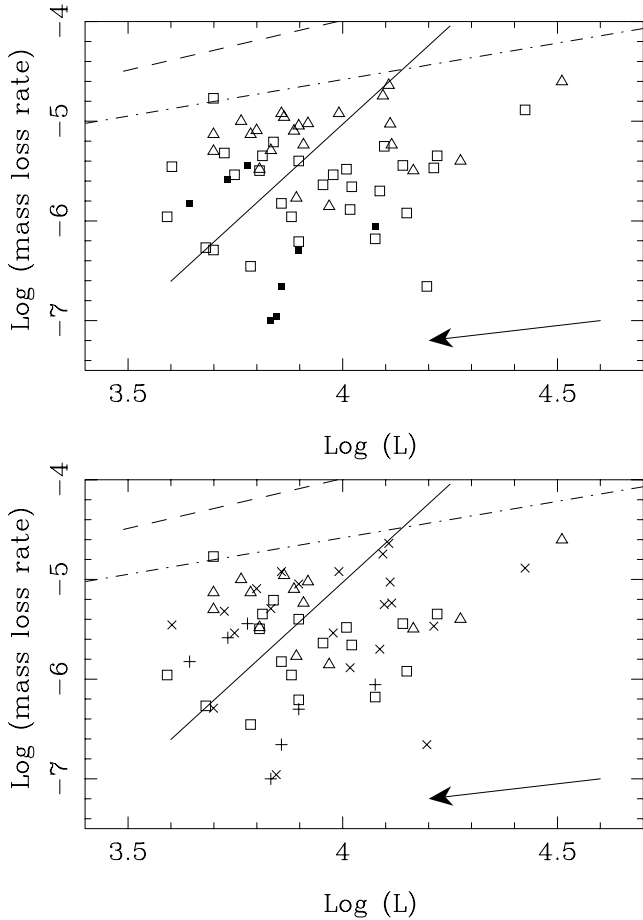


Figure 2 – continued

Fig. 7 demonstrates that the mass-loss rates derived here increase monotonically as the [6.4]–[9.3] colour grows redder. The scatter is substantial for colours bluer than 0.7, with an uncertainty in mass-loss rate of a factor of  $\pm \sim 2$  for a given colour. For colours redder

than 0.7, the scatter is smaller, only about 30 per cent. Given that the mass-loss rate varies by two orders of magnitude in this sample, the rough approximations of the mass-loss rate based on the [6.4]–[9.3] colour are reasonable.



**Figure 3.** Mass-loss rate versus luminosity. SMC objects are indicated by the (open and filled) squares and LMC objects are indicated by (open) triangles. Open symbols are stars with Mira-like pulsation amplitudes; filled symbols are stars either without Mira-like pulsation amplitudes or without any information about their pulsation properties. In the bottom panel, all stars with *non-regular* pulsation (crosses) or without any information about pulsation properties (pluses) have been marked. The arrow indicates the effect of changing the luminosity by 1 mag at constant dust optical depth. The solid line is a fit from Groenewegen et al. (1998) derived from Galactic carbon Miras. The dashed and dot-dashed lines indicate, respectively, the empirical observed maximum limit and the classical limit [ $\sim L/(c v_{\text{exp}})$ ] to the mass-loss rate from van Loon et al. (1999b).

## 5.2 The colours of carbon stars

Many of the selections of AGB stars to be observed by *SST* have been based on the 2MASS-MSX colour-colour diagram by Egan et al. (2001). In that picture, the early carbon-rich AGB stars in their class 5c have colours within the ranges  $0.5 < H - K < 1.25$ ,  $0.2 < K - A < 1.5$ , and  $1.4 < J - K < 1.75$ , while the C-rich late AGB stars in class 6a have  $1.5 \leq K - A < 3.75$  and  $0.8 < H - K \leq 1.5$ .

Based on the sample at our disposal, we can now conclude that the colour range proposed by Egan et al. for selecting C-stars was much too restrictive, especially in  $(K - A)$ . Fig. 8 shows the  $(J - K) - (K - A)$  and  $(H - K) - (K - A)$  2MASS-MSX colour-colour diagrams with the 60 carbon stars plotted (also see Zijlstra et al. 2006). The colours are synthetic colours based on the final dust model for the SEDs and IRS spectra and convolved with the appropriate filter curves (see Groenewegen 2006 for details). The carbon stars in the present sample span a wide range in colour, from

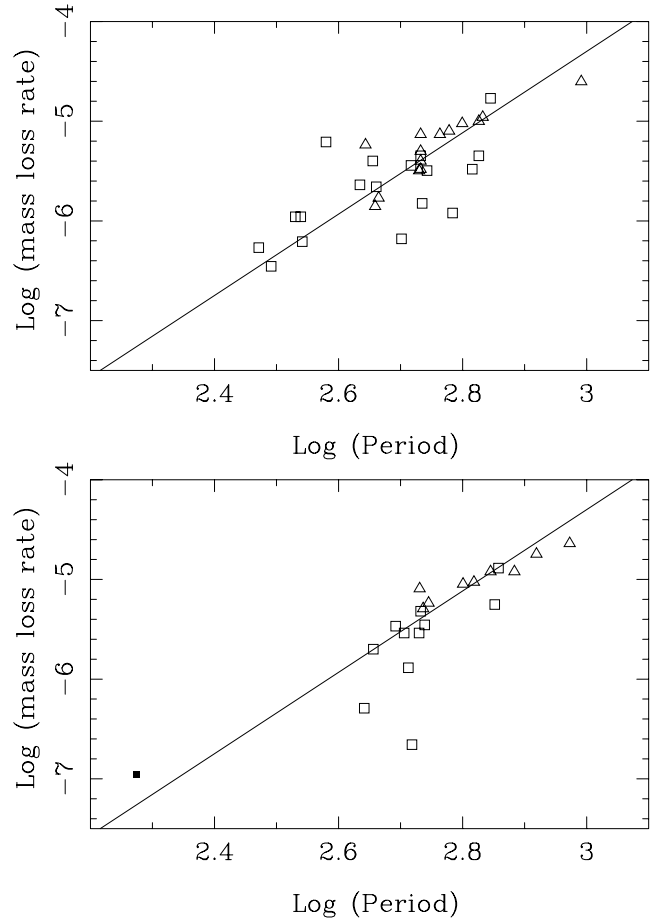


**Figure 4.** Mass-loss rate versus log (period). SMC objects are indicated by the (open and filled) squares and LMC objects are indicated by the triangles. Open symbols are stars with Mira-like pulsation amplitudes and filled symbols are stars with SR-like pulsation amplitudes. In the top panel, the stars with *regular* pulsation [marked by a star (\*) in Table 1] and in the bottom panel the stars with *non-regular* pulsation are plotted. The solid line is a fit from Groenewegen et al. (1998) derived from Galactic carbon Miras.

$(J - K) \approx 1.5$  (which is a well-known selection criterion, e.g. Cioni & Habing 2003) to  $(K - A) = 10$ . Buchanan et al. (2006), using a smaller sample of carbon stars, assign again a too small box in colour space, from  $(J - K) = 3$  to  $(K - A) = 8$ .

Fig. 9 shows the  $[8 - 24] - (H - [5.8])$  and  $(H - K) - (K - [5.8])$  2MASS-*SST* colour-colour diagrams for the sources, similar to Buchanan et al., who plot this for a variety of classes of evolved stars. Compared to their location of the C-stars our, larger, sample extends in  $(H - K)$  colour (from 0.5 to 4, compared to 1.1 to 2.7 in Buchanan et al.) and redder  $(K - [5.8])$  colours (8, compared to 6 in Buchanan et al.).

## 5.3 Dust properties

The SiC/AMC ratio is small. For most stars, a ratio of 2 per cent fits the data, but the error bar is of the order of 2 per cent as well. For only a few stars, a clear SiC feature is present (GM 780 with 8 per cent, IRAS 05360 with 6 per cent). For Galactic carbon stars, a decrease of the SiC/AMC ratio with redder *IRAS* colour is observed, from 6–8 per cent at  $10^{-6} M_{\odot} \text{ yr}^{-1}$  to  $\sim 0$  per cent for mass-loss rates  $\sim 5 \times 10^{-5} M_{\odot} \text{ yr}^{-1}$  and larger (Groenewegen 1995a; Groenewegen et al.

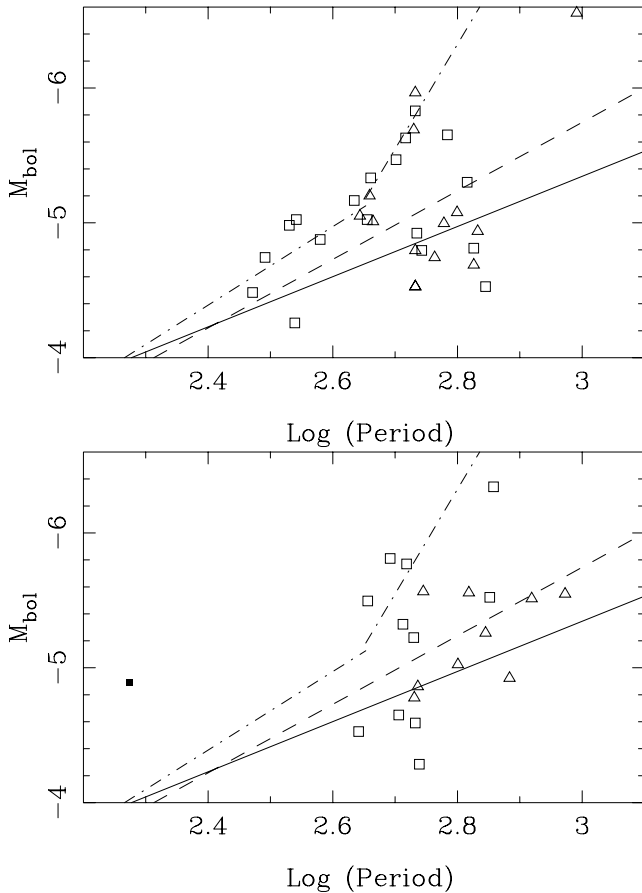


**Figure 5.** Absolute bolometric magnitude versus period. SMC objects are indicated by the (open and filled) squares and LMC objects are indicated by the triangles. Open symbols are stars with Mira-like pulsation amplitudes and filled symbols are stars with SR-like pulsation amplitudes. In the top panel, the stars with *regular* pulsation [marked by a star (★) in Table 1], and in the bottom the stars with *non-regular* pulsation, are plotted. The solid line is an extrapolation of the *PL*-relation derived by Feast et al. (1989) for carbon Miras with periods below 420 d, assuming an LMC distance of 50 kpc, while the dashed line is a C-star *PL*-relation based on LMC stars with periods up to 900 d from Whitelock et al. (2006). The dot-dashed line represents the *PL*-relation below and above 450 d derived by Hughes & Wood (1990) for Mira and SR variables in the LMC.

1998). That the SiC/AMC ratio is smaller in the SMC and LMC compared to that in the Galaxy was also noted by Zijlstra et al. (2006), Sloan et al. (2006) and Lagadec et al. (2006).

#### 5.4 A change of mass-loss rate with time

As can be noted in several SEDs, most notably in MSX SMC 033 and MSX SMC 044, the IRS spectrum lies clearly below the SED predicted by the model. To a lesser extent, this is also observed in MSX SMC 232, MSX SMC 202, MSX SMC 200, *ISO* 00548, *ISO* 00573, *ISO* 01019, NGC 419 IR1, LEGC 105 and RAW 960. Curiously, or interestingly, these are all sources in the SMC. The phenomenon seems not present among LMC sources in the present sample.

As the model flux at the longest wavelengths is too high, one way to decrease the dust emission is to decrease the mass-loss rate some time in the past. As a test, the most extreme example of such

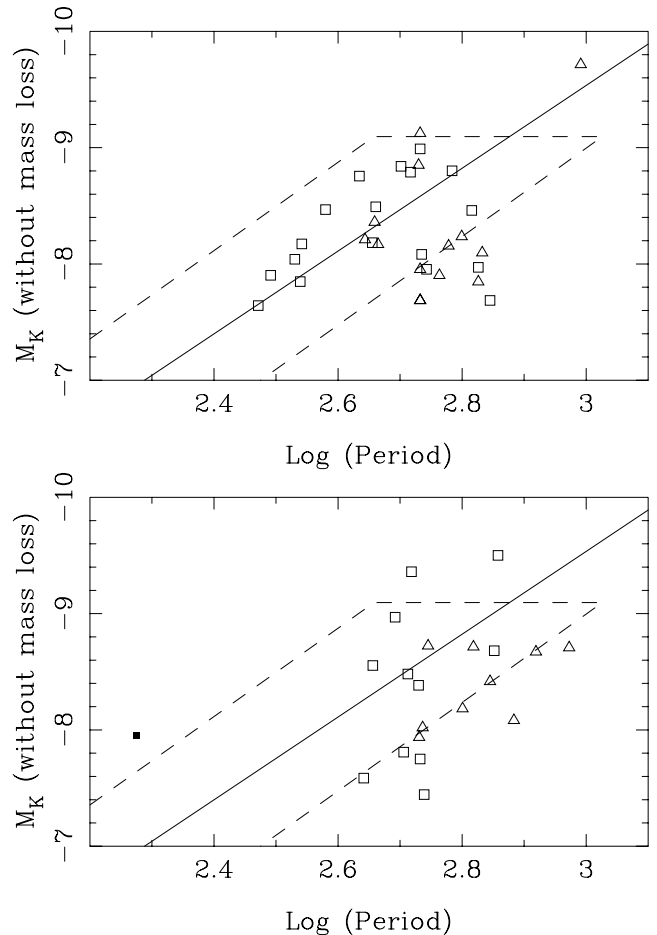


**Figure 6.** Dust-corrected *K* magnitude versus period. SMC objects are indicated by the (open and filled) squares and LMC objects are indicated by the triangles. Open symbols are stars with Mira-like pulsation amplitudes and filled symbols are stars with SR-like pulsation amplitudes. In the top panel, the stars with *regular* pulsation [marked by a star (★) in Table 1], and in the bottom the stars with *non-regular* pulsation, are plotted. The solid line is the *K*-band *PL*-relation from Groenewegen & Whitelock (1996) for stars up to periods of 500 d. The dashed region corresponds to box ‘C’ in Groenewegen (2004), defining the location of the large-amplitude variables (see also Wood et al. 1983).

a time-dependent mass-loss rate is used in the following example: a constant recent mass-loss rate, and zero mass loss in the past, parametrized by changing the outer radius of the dust shell.

Fig. 10 shows the SEDs for MSX SMC 033 and MSX SMC 044 with, from top to bottom,  $R_{\text{outer}}/R_{\text{inner}} = 10, 5, 3$  (for MSX SMC 033) and 10, 3, 2 (MSX SMC 044). The best fits are obtained for, respectively,  $R_{\text{outer}}/R_{\text{inner}} = 5$  and 3.

The corresponding mass-loss rates and luminosities for the best fits are  $5.5 \times 10^{-6} M_{\odot} \text{ yr}^{-1}$  and  $7800 L_{\odot}$  for MSX SMC 044, and  $4.5 \times 10^{-6} M_{\odot} \text{ yr}^{-1}$  and  $14600 L_{\odot}$  for MSX SMC 033. The dust temperature at the outer radius is 410 K (for MSX SMC 033) and 470 K (MSX SMC 044), corresponding to 25 and 35 stellar radii, respectively.

This is roughly consistent with the absence of MgS in all sources which display a SED suggestive of an increase of mass loss with time, as it is suggested that MgS grows as a surface on pre-existing grains (Nuth et al. 1985) at temperatures between around 600 and 300 K (Zijlstra et al. 2006).

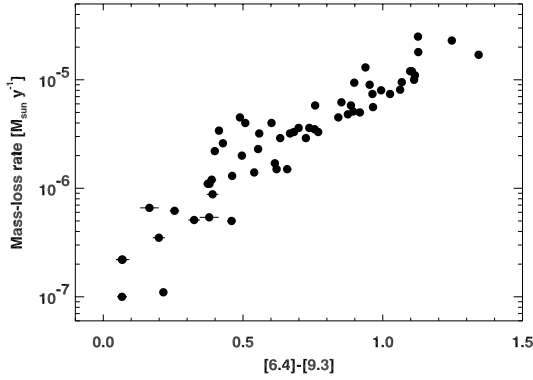


**Figure 7.** Mass-loss rate versus [6.4–9.3] colour.

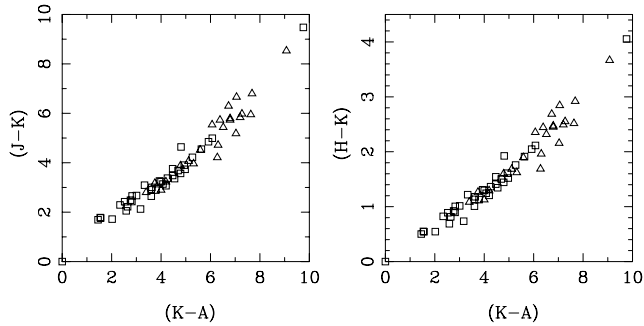


**Figure 8.** 2MASS/MSX colour–colour diagram. SMC objects are indicated by the squares and LMC objects are indicated by the triangles.

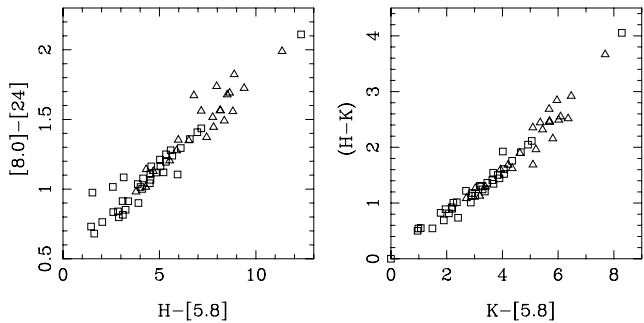


**Figure 9.** 2MASS/SST colour–colour diagram. SMC objects are indicated by the squares and the LMC objects are indicated by the triangles.

The flow time-scale from the star to the outer radius is 45 ( $10 \text{ km s}^{-1}/v_{\text{exp}}$ ) and 23 ( $10 \text{ km s}^{-1}/v_{\text{exp}}$ ) yr for MSX SMC 033 and 044, respectively.

Although the adopted mass-loss rate with time is in all likelihood not unique, and mass-loss rate laws that are continuous in time can be constructed that would also fit the SED, they would need to involve a change of  $\dot{M}$  on a similar time-scale as derived with our simple model.

As a second test, a mass-loss rate law of the form

$$\dot{M} = \frac{\dot{M}_0}{(1 - t/t_0)^\alpha} \quad (2)$$

is tried, where  $t$  is the flow-time-scale from the stellar surface to a radial point in the wind. Values for  $\alpha$  between 0.5 and 1 have been proposed for such a law (Baud & Habing 1983; Bedijn 1987; van der Veen 1989) and a value of 0.75 has been adopted here. Fig. 11 shows the SED for MSX SMC 033 when this mass-loss rate law is tuned

to give a factor of 4 increase over the past 20 yr to a present-day value of  $1.7 \times 10^{-5} M_\odot \text{ yr}^{-1}$ .

An alternative explanation for a changing  $\dot{M}$  is a different absorption coefficient compared to the default in the mid-IR. Although this cannot be formally ruled out, this is not considered a viable explanation as it would require the ad hoc assumption that the AMC absorption coefficient can differ on a star-by-star basis. A second alternative could be deviations from spherical symmetry.

Mass-loss variations on a time-scale of decades have been observed previously close to the central stars of CW Leo and a few other stars (Mauron & Huggins 1999, 2000, 2006). These mass-loss variations are visible in scattered light as multiple-shells and spiral structures, and are consistent with the direct or indirect effects of a binary companion (Mauron & Huggins 2000, 2006).

On the other hand, these shells occur regularly and the overall shape of these SEDs can still be described well by a constant mass-loss rate and a  $1/r^2$  density distribution. If the phenomenon we observe were related to binary interaction, then it implies much longer binary periods.

An alternative explanation would be that these stars are caught in the act of a thermal pulse, at high luminosity and mass-loss rate. As this phase lasts of the order of 1 per cent of the thermal pulse cycle, the probability to have at least two cases in a sample of 60 objects is about 12 per cent.

Another source where the SED is not well described by a constant mass-loss rate is MSX SMC 060. Here, one observes the inverse, i.e. the shape of the SED suggests a mass-loss rate which was larger in the past.

A mass-loss rate of the form

$$\dot{M} = \dot{M}_0 \exp(-t/t_0) \quad (3)$$

was fitted with a maximum of  $10^{-4} M_\odot \text{ yr}^{-1}$ .

Fig. 11 shows a model with  $t_0 = 1000$  yr and a present-day mass loss of  $6.3 \times 10^{-6} M_\odot \text{ yr}^{-1}$  that reasonably fits the data. Values for  $t_0$  that differ by a factor of 2 give clearly poorer fits.

## 6 SUMMARY AND CONCLUSIONS

The SST IRS 5–35  $\mu\text{m}$  spectra and quasi-simultaneous *JHKL* photometry of 60 carbon stars in the SMCs and LMCs have been fitted with a dust radiative transfer model. Light curves for 36 objects could be retrieved from the MACHO and OGLE data bases, and periods could be derived for all but two. Only 21 stars show regular pulsation however. Periods were obtained from other sources for another 19 objects.

From the modelling of the SEDs, the luminosity and mass-loss rate are derived (under the assumption of a fixed expansion velocity and dust-to-gas ratio), and the ratio of SiC to AMC dust is estimated.

This ratio is smaller than observed in Galactic carbon stars, as already noted by Zijlstra et al. (2006) and Sloan et al. (2006).

The mass-loss rates are plotted against pulsation period and luminosity, and compared to relations derived for Galactic carbon stars. The fact that the luminosities are based on single-epoch data introduces significant scatter (more than an order of magnitude spread in mass-loss rate for a given luminosity) so that no firm conclusions can be drawn. The mass-loss rates for the MC objects roughly scatter around the mean relation for Galactic C-stars.

The situation is better defined when mass loss is plotted against period. The stars that show regular pulsation, and most of the stars with less well-defined light curves, have mass-loss rates that are in agreement with that observed in Galactic carbon stars. An uncertainty in this analysis is the adoption of a constant velocity

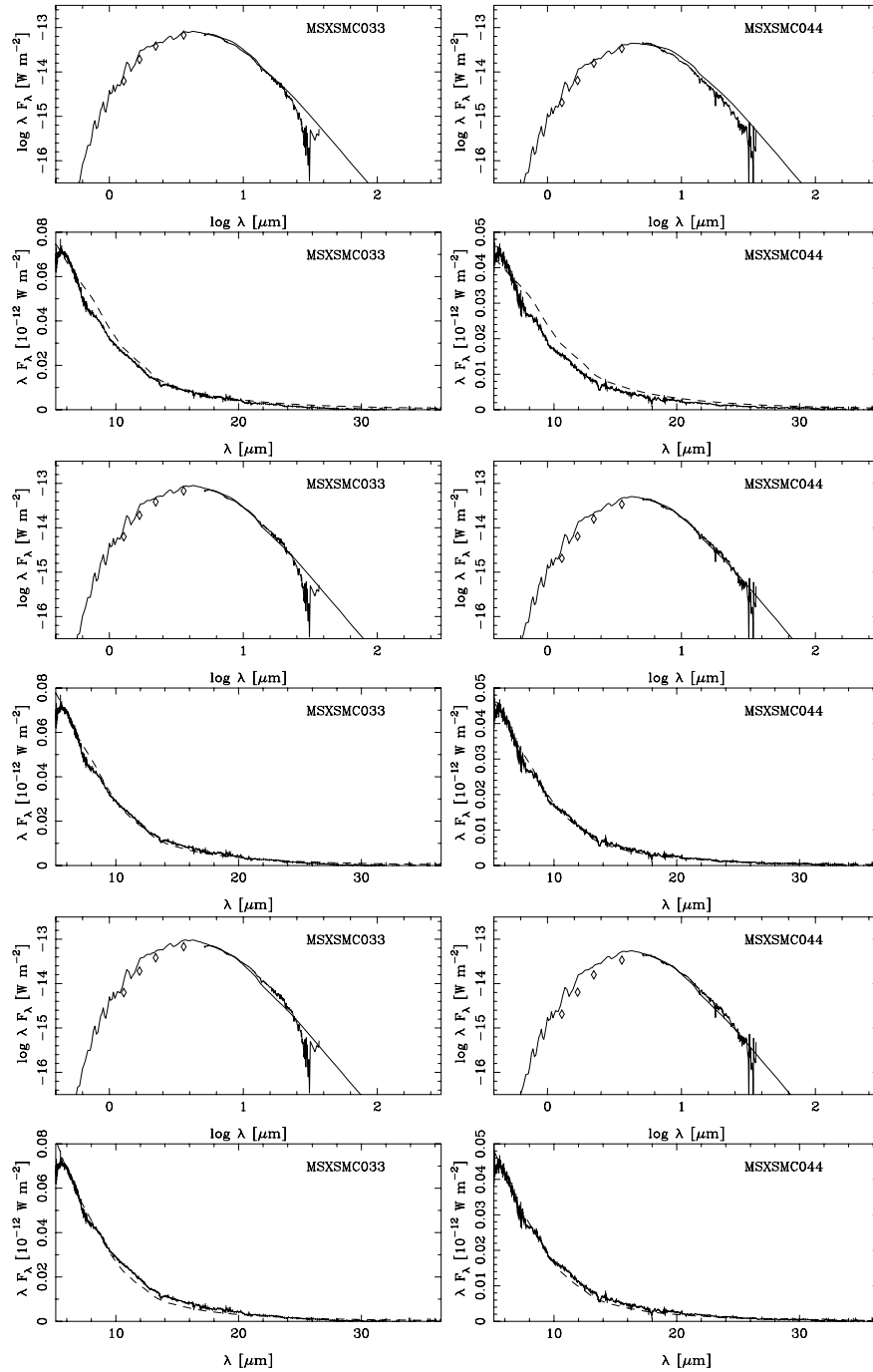


**Figure 10.** The effect of a reduced outer radius with, from top to bottom,  $R_{\text{outer}}/R_{\text{inner}} = 10, 5, 3$  (for MSX SMC 033) and  $10, 3, 2$  (MSX SMC 044).

and dust-to-gas ratio for the MC sources. No firm independent determinations exist for MC AGB stars for these quantities and therefore mean values observed in Galactic stars had to be adopted. Only when the Atacama Large Millimeter Array becomes available will it be possible to observe the CO rotational lines in a few dozen AGB stars (including the reddest and luminous stars in the present sample) and directly measure the expansion velocity and gas mass-loss rate (Groenewegen 1995b).

One of the surprising results of this study is that for a few sources the SED is not well fitted by the model at the longer wavelengths. There is one case where the data lie above the model predictions,

and half a dozen cases where the data clearly fall below the model. All these sources happen to be in the SMC.

Several interpretations are offered, but none of them seems to be entirely satisfactory. One possibility is to change the absorption coefficients of the dust at longer wavelengths. An argument against this is that for the majority of stars very good fits are obtained with the standard assumption of AMC dust (including previous work on Galactic objects), so any deviation from this to fit a particular SED would be rather ad hoc.

A distinct possibility, but one which we are unable to quantify here, is the presence of a disc, or, more generally, a deviation

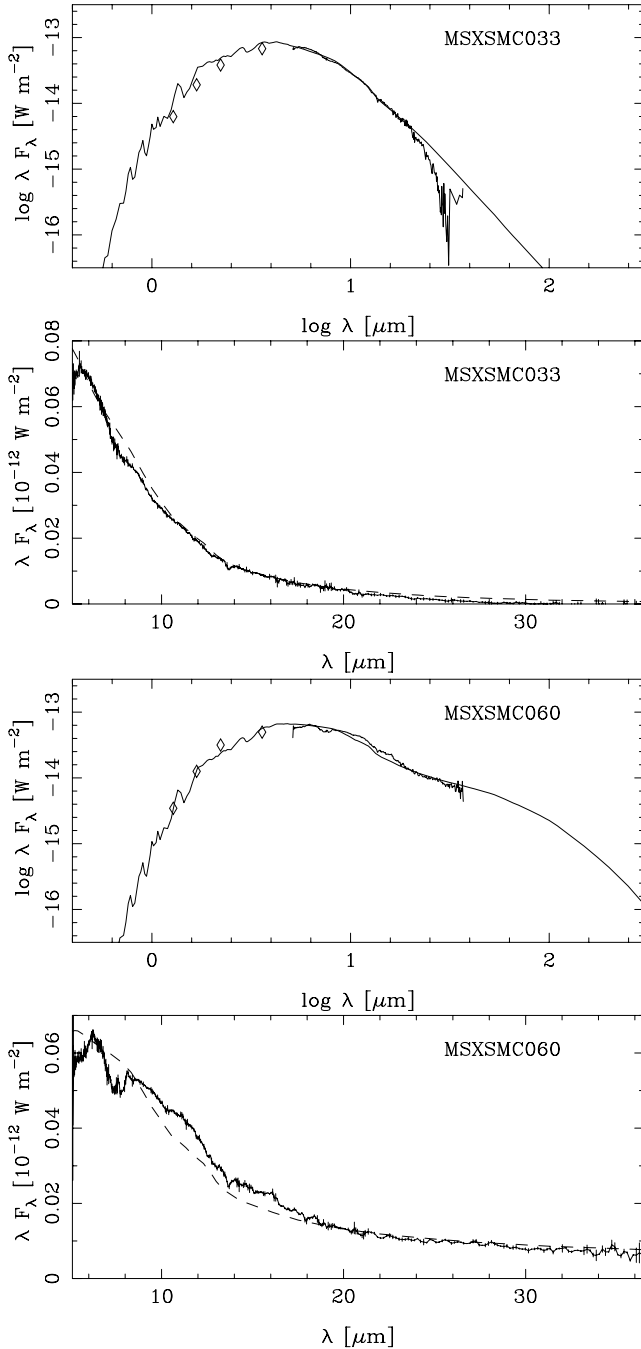


**Figure 11.** The effect of a changing mass loss with time in MSX SMC 033 and MSX SMC 060 (see text for details on the adopted mass-loss rate laws).

from the assumption of spherical symmetry assumed in the model calculations.

A possibility, which is investigated in a more quantitative way, is mass-loss variations in time, which one knows can occur in AGB stars on different time-scales. For one object, we derive that the mass-loss rate has decreased with time on a typical time-scale of  $10^3$  yr, for two other extreme cases we find an increase in mass-loss rate by a factor of few over a time-scale of a few decades. An argument against the hypothesis of mass-loss rate variations with time is the associated time-scales. To have two very clear (and a few more less clear) cases of mass-loss variations on such a short time-

scale in 60 objects in total is not likely. A possible way to verify this scenario would be to observe the spectra of these stars near the end of the lifetime of *Spitzer* and look for variations over the few year baseline.

Finally, we note that in a forthcoming paper we will derive mean luminosities from monitoring observations of the objects studied here. We will also derive properties such as stellar mass and we will examine the dependence of mass-loss rate on the various properties of the central stars.

## ACKNOWLEDGMENTS

This research has made use of the SIMBAD data base, operated at CDS, Strasbourg, France.

PRW has been partially supported during this research by a discovery grant from the Australian Research Council.

This paper utilizes public domain data originally obtained by the MACHO Project, whose work was performed under the joint auspices of the US Department of Energy, National Security Administration by the University of California, Lawrence Livermore National Laboratory under contract No. W-7405-Eng-48, the National Science Foundation through the Center for Particle Astrophysics of the University of California under cooperative agreement AST-8809616, and the Mount Stromlo and Siding Spring Observatory, part of the Australian National University.

## REFERENCES

- Alcock C. et al., 1997, *ApJ*, 486, 697  
 Baud B., Habing H. J., 1983, *A&A*, 127, 73  
 Bedijn P. J., 1987, *A&A*, 186, 136  
 Buchanan C. L., Kastner J. H., Forrest W. J., Hrivnak B. J., Sahai R., Egan M., Frank A., Barnbaum C., 2006, *AJ*, 132, 1890  
 Cioni M.-R. L., Habing H. J., 2003, *A&A*, 402, 133  
 Dodion J., 2003, MSc thesis, Univ. Leuven  
 Egan M. P., Van Dyk S. D., Price S. D., 2001, *AJ*, 122, 1844  
 Feast M. W., Glass I. S., Whitelock P. A., Catchpole R. M., 1989, *MNRAS*, 241, 375  
 Goebel J. H., Moseley S. H., 1985, *ApJ*, 290, L35  
 Groenewegen M. A. T., 1993, PhD thesis, Chapter 5, Univ. Amsterdam  
 Groenewegen M. A. T., 1995a, *A&A*, 293, 463  
 Groenewegen M. A. T., 1995b, in Shaver P., ed., *Science with Large Millimetre Arrays*. Springer-Verlag, Berlin p. 164  
 Groenewegen M. A. T., 2004, *A&A*, 425, 595  
 Groenewegen M. A. T., 2005, *A&A*, 439, 559  
 Groenewegen M. A. T., 2006, *A&A*, 448, 181  
 Groenewegen M. A. T., Blommaert J. A. D. L., 1998, *A&A*, 332, 25  
 Groenewegen M. A. T., Whitelock P. A., 1996, *MNRAS*, 281, 1347  
 Groenewegen M. A. T., Whitelock P. A., Smith C. H., Kerschbaum F., 1998, *MNRAS*, 293, 18  
 Groenewegen M. A. T., Blommaert J. A. D. L., Cioni M.-R. L., Okumura K., Habing H. J., Trams N. R., van Loon J. Th., 2000, *Mem. Soc. Astron. Ital.*, 71, 639  
 Hony S., Bouwman J., 2004, *A&A*, 413, 981  
 Houck J. R. et al., 2004, *ApJS*, 154, 18  
 Hughes S. M. G., Wood P. R., 1990, *AJ*, 99, 784  
 Lagadec E., Zijlstra A. A., Sloan G. C. et al., 2006, *MNRAS*, in press (astro-ph/0611071)  
 Loidl R., Lançon A., Jørgensen U. G., 2001, *A&A*, 371, 1065  
 Loup C., Zijlstra A. A., Waters L. B. F. M., Groenewegen M. A. T., 1997, *A&AS*, 125, 419  
 Loup C. et al., 1999, in Cox P., Kessler M. F., eds, *The Universe as Seen by ISO*. ESA-SP 427, p. 369  
 Marigo P., 2002, *A&A*, 387, 507

- Marshall J. R., van Loon J. Th., Matsuura M., Wood P. R., Zijlstra A. A., Whitelock P. A., 2004, *MNRAS*, 355, 1348
- Matsuura M. et al., 2005, *A&A*, 434, 691
- Matsuura M. et al., 2006, *MNRAS*, 371, 415
- Mauron N., Huggins P. J., 1999, *A&A*, 349, 203
- Mauron N., Huggins P. J., 2000, *A&A*, 359, 707
- Mauron N., Huggins P. J., 2006, *A&A*, 452, 257
- McGregor P. J., 1994, *PASP*, 106, 508
- McGregor P. J., Hart J., Hoadley D., Bloxham G., 1994, in McLean I., ed., *Infrared Astronomy with Arrays*. Kluwer, Dordrecht, p. 299
- Nishida S., Tanabé T., Nakada Y., Matsumoto S., Sekiguchi K., Glass I. S., 2000, *MNRAS*, 313, 136
- Nuth J. A., Moseley S. H., Silverberg R. F., Goebel J. H., Moore W. J., 1985, *ApJ*, 290, L41
- Olivier E. A., Wood P. R., 2003, *ApJ*, 584, 1035
- Pégourié B., 1988, *A&A*, 194, 335
- Raimondo G., Cioni M.-R. L., Rejkuba M., Silva D. R., 2005, *A&A*, 438, 521
- Reid N., 1991, *ApJ*, 382, 143
- Reid N., Glass I. S., Catchpole R. M., 1988, *MNRAS*, 232, 53
- Rouleau F., Martin P. G., 1991, *ApJ*, 377, 526
- Schwering P. B. W., 1989, *A&AS*, 79, 105
- Schwering P. B. W., Israel F. P., 1989, *A&AS*, 79, 79
- Sloan G. C., Kraemer K. E., Matsuura M., Wood P. R., Price S. D., Egan M. P., 2006, *ApJ*, 645, 1118
- Sperl M., 1998, *Comm. Astroseismol.*, 111, 1
- Stellingwerf R. F., 1978, *ApJ*, 224, 953
- Tanabé T., Kucinkas A., Nakada Y., Onaka T., Sauvage M., 2004, *ApJS*, 155, 401
- Trams N. R. et al., 1999, *A&A*, 346, 843
- van der Veen W. E. C. J., 1989, *A&A*, 210, 127
- van Loon J. Th., Zijlstra A. A., Whitelock P. A., Waters L. B. F. M., Loup C., Trams N. R., 1997, *A&A*, 325, 585
- van Loon J. Th., Zijlstra A. A., Groenewegen M. A. T., 1999a, *A&A*, 346, 805
- van Loon J. Th., Groenewegen M. A. T., de Koter A., Trams N. R., Waters L. B. F. M., Zijlstra A. A., Whitelock P. A., Loup C., 1999b, *A&A*, 351, 559
- van Loon J. Th., Zijlstra A. A., Bujarrabal V., Nyman L.-Å., 2001, *A&A*, 368, 950
- van Loon J. Th., Cioni M.-R. L., Zijlstra A. A., Loup C., 2005, *A&A*, 438, 273
- van Loon J. Th., Marshall J. R., Cohen M., Matsuura M., Wood P. R., Yamamura I., Zijlstra A. A., 2006, *A&A*, 447, 971
- Werner M. W. et al., 2004, *ApJS*, 154, 1
- Whitelock P. A., Feast M. W., Menzies J. W., Catchpole R. M., 1989, *MNRAS*, 238, 769
- Whitelock P. A., Feast M. W., van Loon J. Th., Zijlstra A. A., 2003, *MNRAS*, 342, 86
- Whitelock P. A., Feast M. W., Marang F., Groenewegen M. A. T., 2006, *MNRAS*, 369, 751
- Wood P. R., 1998, *A&A*, 338, 592
- Wood P. R., Bessell M. S., Fox M. W., 1983, *ApJ*, 272, 99
- Wood P. R., Whiteoak J. B., Hughes S. M. G., Bessell M. S., Gardener F. F., Hyland A. R., 1992, *ApJ*, 397, 552
- Wood P. R., Olivier E. A., Kawaler S. D., 2004, *ApJ*, 604, 800
- Zebrun K. et al., 2001, *Acta Astron.*, 51, 317
- Zijlstra A. A., Loup C., Waters L. B. F. M., Whitelock P. A., van Loon J. Th., Guglielmo F., 1996, *MNRAS*, 279, 32
- Zijlstra A. A. et al., 2006, *MNRAS*, 370, 1961

This paper has been typeset from a  $\text{\TeX}/\text{\LaTeX}$  file prepared by the author.